American Mineralogist, Volume 80, pages 1229–1251, 1995

An experimental study of element partitioning among biotite, muscovite, and coexisting peraluminous silicic melt at 200 MPa (H_2O)

Jonathan Icenhower, David London
School of Geology and Geophysics, University of Oklahoma, Norman, Oklahoma 73019, U.S.A.

Abstract

H_2O-saturated experiments with synthetic metapelite compositions (muscovite-quartz-albite and muscovite-quartz-albite-biotite ± aluminum silicate ± cordierite) performed over the temperature interval of 600–750 °C at 200 MPa (H_2O) reveal that partial fusion commences at 625 °C along the metastable extension of the reaction muscovite + quartz + albite + H_2O = melt + aluminum silicate. Biotite is stable over the entire temperature interval, although it reacts progressively to hercynite + melt at the high end of the temperature range. Muscovite that survives initial melting breaks down to corundum + orthoclase between 700 and 725 °C. Minor corundum and aluminum silicate are present at 650 °C, whereas corundum with a large sapphire (Fe + Ti) component is present at and above 700 °C. Finally, corundum and hercynite exist with orthoclase-rich feldspar and remaining biotite at 750 °C. The normative composition of melt at the minimum is approximately $Ab_{30}Or_{15}Ms_{20}Qtz_{35}$ (in weight percent) without other minor components (e.g., cryolite). Both muscovite and its equivalent orthoclase + corundum assemblage contribute substantial excess Al to melt, bringing the value of the Al saturation index (ASI) of melt to 1.4. Li, Rb, Cs, and F are strongly enriched in melts because of the continuous reaction and reequilibration of biotite and muscovite over the temperature interval. Concentrations of the femic components (TiO_2 + FeO + MgO + MnO) are low (<1 wt%) but rise with temperature primarily because of increasing solubilities of FeO in melt. Calculated partition coefficients, $D(M)^{Bt/gl}$, between biotite (Bt) and glass (gl) for the element M show that $D(Li)^{Bt/gl}$ (1.7–1.0), $D(Ba)^{Bt/gl}$ (~14–6), and $D(F)^{Bt/gl}$ (2.5–1.5) all decrease with increasing temperature, whereas partition coefficients for Sr (≈0.04), Rb (≈2.0), and Cs (≈0.4) remain constant with temperature over a large range of concentrations. Partition coefficients for muscovite (Ms) were also determined at 650 °C; $D(M)^{Ms/gl} \approx$ 0.8 (Li), 3–6 (Ba), 1.6 (Rb), 0.05 (Sr), 0.3 (Cs), and 1.8 (F). These results, together with other data for feldspar, suggest that Rb, Cs, and Ba become strongly fractionated from one another during anatexis of aluminous metasediments and the ensuing crystallization of melts. Finally, the low partition coefficients for F between micas (biotite or muscovite) and melt indicate that F-rich melts can be generated by the incipient hydrous anatexis of aluminous metasediments; models that invoke remelting of a dehydrated protolith to generate such F-rich melts may not be necessary.

Introduction

Partitition coefficients for major and trace elements among biotite, muscovite, and coexisting silica-rich melts have figured prominently in models for anatexis of aluminous metasediments and the evolution of peraluminous granitic suites (e.g., de Albuquerque, 1975; Nabelek, 1986; Walker et al., 1986, 1989; Harris and Inger, 1992; Jolliff et al., 1992; Hall et al., 1993). The behavior of major elements and especially trace large-ion lithophile elements (LILEs, including Li, Rb, Cs, Ba, and Sr) can provide important petrogenetic information on probable melting reactions and, hence, the lithology and proportions of phases in the source rocks if the partition coefficients for these elements between melt and crystalline phases are known. Because other elements important in constraining such processes (e.g., REEs, Zr, Th, and U) are typically harbored by accessory phases with highly variable solubilities in felsic melts (e.g., Hogan and Sinha, 1991; Watson and Harrison, 1983; Watson and Capobianco, 1981; Rapp and Watson, 1986), partition coefficient data for the LILEs become more important. As summarized below, the values and variability of these partition coefficients involving major phases and peraluminous melt are poorly constrained.

In this study, we have determined from experiments the partition coefficients for major and minor elements (Fe, Mg, Mn, Ti, and F), normally trace LILEs (Li, Rb, Cs, Ba, and Sr), and other elements among biotite, white mica, and peraluminous melt produced by hydrous partial melting of the assemblage quartz + albite + muscovite + biotite ± cordierite ± aluminum silicate. In

0003–004X/95/1112–1229$02.00

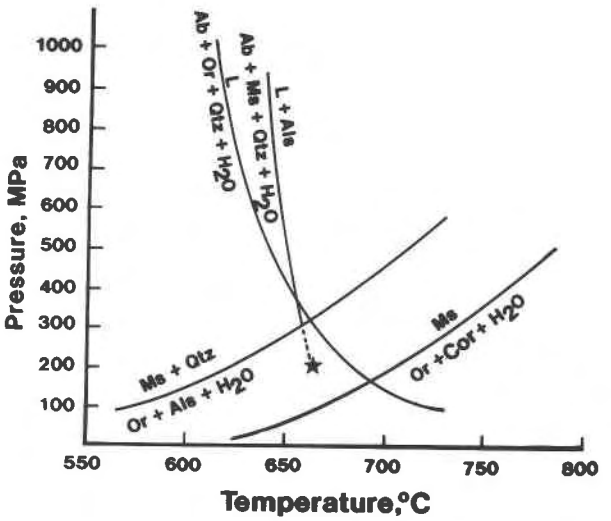

Fig. 1. Phase relations for peraluminous granitic systems in terms of pressure and temperature, after Storre and Karotke (1971). The dashed line is the metastable extension of the reaction albite + muscovite + quartz + H_2O = melt + aluminum silicate to 200 MPa (2 kbar) pressure, the conditions of our experiments (star). The H_2O-saturated haplogranite solidus (quartz + albite + orthoclase + H_2O = melt) and the subsolidus second sillimanite isograd (quartz + muscovite = orthoclase + aluminum silicate + H_2O) were determined by Merrill et al. (1970) and Althaus et al. (1970), respectively. The terminal muscovite reaction, muscovite = orthoclase + corundum + H_2O, was delineated by Yoder and Eugster (1955). Abbreviations: Ab = albite, Als = aluminum silicate, Ms = muscovite, Qtz = quartz, Or = orthoclase, L = melt, Cor = corundum.

companion papers (Icenhower and London, in preparation), we present similar results for feldspar and for garnet + cordierite + biotite + andalusite assemblages. The chosen starting assemblage represents a reasonable but simple analog of aluminous gneisses and metapelites that experience first melting at pressures above and temperatures below the reaction muscovite + quartz = orthoclase + aluminum silicate; i.e., still in the field of stability for muscovite + quartz (Fig. 1) and with initially orthoclase-absent starting compositions. By control of bulk composition, we were able to explore the melting and crystallization of the starting assemblage quartz + albite + muscovite + biotite at low P (200 MPa), so that the partitioning results are applicable to crystallization of melts that have migrated to shallow crustal levels. We elected to conduct these experiments at saturation in H_2O, knowing that the compositions of fluid phases in typical semi- or metapelitic schist and gneiss sequences at conditions of the upper amphibolite facies of metamorphism are not pure H_2O but are diluted by CO_2 and CH_4 as controlled by T, f_{O_2}, and graphite in the source rocks. Saturation in H_2O helped to produce large quantities of melt, which facilitated accurate analysis of crystalline and glass phases, at low T. An additional rationale was to examine a limiting case of typical hydrous melting at lowest temperatures toward an appraisal of the conditions of anatexis that might produce melts corresponding both to migmatites and to chemically evolved (i.e., rare-alkali–rich) pegmatites by low degrees of anatexis (e.g., Stewart, 1978). The resulting partition coefficients represent a body of data that may be applied, with caveats cited, to any general or specific circumstance of melting or crystallization involving micas and peraluminous melts. In this paper, we utilize these results to discuss (1) the bulk compositions of melts derived from the anatexis of aluminous gneissic or pelitic protoliths, (2) the role and reaction of biotite at the onset of low-temperature melting, and (3) the trace-element signatures of melts derived from assemblages bearing muscovite + biotite.

Previous work and rationale for this study

Although numerous investigators have reported partition coefficient data for metaluminous and peralkaline silicic systems (e.g., Philpotts and Schnetzler, 1970; Hanson, 1978; Higuchi and Nagasawa, 1969; Arth, 1976; Mahood and Hildreth, 1983), few data exist for peraluminous magmas. Nash and Crecraft (1985) presented partitioning data for Ba and Rb between plagioclase, potassium feldspar, biotite, and garnet and coexisting high-silica glass; only one of these compositions is peraluminous. Pichavant et al. (1988) reported trace-element compositions of biotite, muscovite, and glass from the peraluminous Macusani volcanic field, Peru. Biotite and muscovite analyses were, however, conducted on mineral separates, not in situ, and not necessarily involving crystal-glass phases at equilibrium. Walker et al. (1986, 1989) estimated muscovite partition coefficients by dividing average biotite-melt partition coefficients (determined predominantly on natural metaluminous compositions) into biotite-muscovite element ratios determined by Shearer et al. (1986) in several pegmatites from the Black Hills, South Dakota.

With these references as the principal or sole sources of data, it is evident that crystal-melt partitioning data for the important major and trace constituents of peraluminous systems are not well established, and this fact curtails fruitful investigation of the origins of peraluminous granites, pegmatites, and rhyolites. In addition, the peraluminous compositions of melts produced from the assemblage quartz + albite + muscovite (discussed below) might increase the likelihood of Tschermak substitutions, e.g., $BaAlK_{-1}Si_{-1}$ in micas; thus, crystal-melt partition coefficients in peraluminous systems might be different from those in metaluminous or peralkaline compositions.

Starting materials

Compositions corresponding to synthetic metapelites were made from mixtures of muscovite, albite, and quartz. Muscovite was separated from a recrystallized muscovite + tourmaline schist near a contact with the Strickland-Cramer pegmatite body, Portland, Connecticut (DL sample STK-127). Electron microprobe analyses (EMPA)

TABLE 1. Compositions of starting minerals

	Albite $n = 40$	Muscovite $n = 37$	Biotite $n = 84$	Andalusite $n = 30$	Cordierite $n = 25$
			Weight percent		
SiO_2	68.22(0.25)	45.92(0.28)	40.12(0.84)	36.15(0.16)	48.39(0.25)
TiO_2		0.44(0.15)	1.19(0.14)		*0.04*(0.01)
Al_2O_3	19.95(0.19)	33.83(0.63)	17.56(0.38)	63.65(0.26)	33.72(0.13)
MgO	*0.02*(0.00)	0.76(0.07)	7.25(0.24)		12.56(0.10)
CaO	0.03(0.03)	*0.02*(0.00)	*0.02*(0.01)		*0.02*(0.01)
Li_2O*		0.46	2.17		
MnO		0.21(0.03)	0.23(0.03)	*0.04*(0.01)	0.06(0.02)
Fe_2O_3**			2.26		
FeO	*0.02*(0.00)	2.73(0.14)	8.13(0.61)	0.31(0.02)	2.55(0.07)
NiO		*0.04*(0.01)	*0.04*(0.01)		
SrO	*0.07*(0.03)	0.09(0.09)	0.14(0.15)		
BaO	*0.13*(0.03)	*0.13*(0.06)	*0.13*(0.05)		
Na_2O	11.45(0.13)	0.39(0.04)	*0.02*(0.01)		0.30(0.02)
K_2O	0.21(0.03)	10.69(0.10)	6.78(0.33)		*0.02*(0.01)
Rb_2O	*0.05*(0.00)	*0.05*(0.03)	3.82(0.07)		*0.05*(0.00)
Cs_2O	*0.11*(0.02)	*0.11*(0.03)	3.83(0.59)		*0.11*(0.02)
H_2O†		3.78(0.08)	1.42(0.13)		
F		1.30(0.12)	4.58(0.29)		*0.17*(0.05)
P_2O_5	0.03(0.02)				
Total	100.29	100.45	99.48	100.15	97.97
O = F		99.90	97.55		
			Cations p.f.u.		
Normalization basis	8(O)	24(O,OH,F)	24(O,OH,F)	20(O)	18(O)
Si	2.98	6.27	6.69	3.91	4.90
[4]Al		1.73	1.31		
Ti		0.05	0.15		0.00
[6]Al	1.03	3.71	2.14	8.11	4.03
Mg	0.00	0.15	1.80		1.90
Ca	0.01	0.00	0.00		0.00
Li		0.25	1.59		
Mn		0.02	0.03	0.00	0.00
Fe^{3+}			0.26		
Fe^{2+}	0.00	0.31	1.04	0.03	0.22
Ni		0.00	0.00		
Sr	0.00	0.01	0.00		
Ba	0.00	0.00	0.00		
Na	0.95	0.10	0.00		0.06
K	0.02	1.86	1.44		0.00
Rb	0.00	0.00	0.41		0.00
Cs	0.00	0.00	0.27		0.00
P	0.00				
Total	4.98	14.20	15.67	12.05	11.10
Ab	0.97	Mg′ =	Mg′ =		Mg′ =
Or	0.02	0.31	0.55		0.90
An	0.01				

Note: Numbers in parentheses represent standard errors. Numbers in italics represent detection limits. Blank = not determined.
* Li_2O determined by ICP.
** Fe_2O_3 determined by titration.
† H_2O estimated by stoichiometry.

presented in Table 1 indicate that it is characterized by relatively high concentrations of F (~1.3 wt%) and low TiO_2 (0.44%), MgO (0.76%), FeO (total Fe as FeO) (2.73%), and Na_2O (0.39%). In addition, the muscovite contains ~2275 ppm Li (or ~0.4 wt% Li_2O), as determined by inductively coupled plasma (ICP) techniques. Microprobe analyses of the starting feldspar (Table 1) from Minas Gerais, Brazil, reveal that it is near end-member albite. The quartz is a high-purity electronic grade (kindly provided by Feldspar Corporation, Spruce Pine, North Carolina). Concentrations of SrO, BaO, Rb_2O, and Cs_2O in all three minerals, as determined by electron microprobe, are below their respective detection limits.

The minerals were mixed in weight proportions $Ms_{49}Ab_{27}Qtz_{24}$, which is roughly equivalent to the composition of the eutectic in the system quartz-albite-orthoclase-H_2O at 200 MPa (H_2O) (Tuttle and Bowen, 1958) on the assumption that muscovite melts incongruently to equimolar quantities of orthoclase melt and crystals of aluminum silicate or corundum. The composition of this simple, three-mineral starting powder is tabulated in Table 2 as Synpel 4, for "synthetic metapelite." A second set of starting compositions (Synpel 5, 6, and 7) was produced by mixing ~30% by weight biotite to the quartz-albite-muscovite mixture and by varying the proportions of quartz, albite, and muscovite. These bulk compositions were designed to have one or more phases coexisting with melt: Synpel 5, biotite; Synpel 6, feldspar and biotite; and, Synpel 7, biotite and muscovite. A final composition, Synpel 8, contained the same proportions

TABLE 2. Compositions of starting assemblages (wt%)

	Synpel 4	Synpel 5+	Synpel 6+	Synpel 7+	Synpel 8
Muscovite	49	34	27.5	44.3	42
Quartz	24	17	13.5	12	20
Albite	27	19	29	13.7	23
Biotite	0	30	30	30	15
			Trace element (wt%)		
BaO	0	2	2	2	1
SrO	0	2	2	2	0.5
Rb_2O	0	1.15	1.15	1.15	0.58
Cs_2O	0	1.15	1.15	1.15	0.58

of muscovite, quartz, and albite as Synpel 4 but with half the biotite of Synpel, 5, 6, and 7 (see Table 2) and has a correspondingly lower rare-alkali content, as described below. The melts are quartz-undersaturated at temperatures above the minimum because we are more interested in element partitioning among coexisting micas and feldspars, and one crystalline phase (in this case, quartz) must disappear upon entering a divariant field of crystals + liquid.

The starting biotite is a Li-, Cs-, Rb- and F-rich metasomatic mica from the wall rocks of the Tanco pegmatite, Manitoba (Table 1; Morgan, 1986). In addition, this mica contains ~2.15 wt% Li_2O. We used this mica as a source of Li, Rb, Cs, and F. It is highly unstable at the conditions of our experiments; it reacts (dissolves) almost completely and reprecipitates as a new mica in equilibrium with melt. Thus, there is no problem in distinguishing, by back-scattered electron imaging, relict mica grains from those that have recrystallized and chemically equilibrated with (precipitated from) the melt. Lithophile elements Sr and Ba were added to Synpel 5, 6, and 7 as glasses of celsian ($BaAl_2Si_2O_8$) and slawsonite ($SrAl_2Si_2O_8$). A plus sign denotes experiments that included doping in Sr and Ba (e.g., SP5+1), otherwise a hyphen is used (e.g., SP5-1). Doped Synpel 5, 6, and 7 experiments all contain 2% by weight each BaO and SrO (glasses of celsian and slawsonite) as well as 1.15% each of Rb_2O and Cs_2O (starting biotite). In contrast, all Synpel 8 experiments contain 1% by weight BaO (celsian glass), 0.5% SrO (slawsonite glass), and 0.58% each Rb_2O and Cs_2O (starting biotite). Starting assemblages, as well as Rb_2O, Cs_2O, BaO, and SrO concentrations, are summarized in Table 2.

The bulk compositions were designed to have concentrations of normally trace elements that were measurable with high accuracy by EMPA. Consequently, experiments contained as much as ~2 wt% each of Rb, Cs, Ba, and Sr as oxide components added through minerals (biotite and muscovite) or glasses, as discussed above. The bulk compositions, however, were adjusted to produce large volumes of melt at low temperatures; i.e., to be near minimum. In this way, the high concentrations of LILEs were diluted by the large volume of melt and, depending on the partitioning behavior, the concentrations of LILEs were brought above, but near, the lower limits of detection by EMPA for all mineral-melt pairs.

To assess the validity of the Synpel results at lower (trace) concentrations of elements, the partition coefficients for Li, Rb, Cs, Ba, and Sr were determined between glass and biotite crystallized from an experiment conducted on a vitrophyre from Spor Mountain, Utah (SM-1 of Webster et al., 1987), at 200 MPa (H_2O). The SM-1 vitrophyre contained these same LILEs in the 100–300 ppm range. The biotite-glass pair from SM-1, together with select Synpel products, were analyzed together by secondary ion mass spectrometry (SIMS) microprobe. In summary, the presence of nearly 1 wt% Li_2O in biotite and muscovite produced from Synpel compositions does not appear to affect partition coefficients for the other LILEs (compared with values obtained from SM-1 experiments), and the partition coefficients for the LILEs at high concentrations in Synpel experiments are essentially indistinguishable from those in SM-1 products at the same T.

Seed crystals of either cordierite (India) or andalusite (Brazil) were added to select experiments to assess the stability of these phases at the P-T-composition conditions. Compositions of these seed crystals are given in Table 1.

EXPERIMENTAL METHODS

Mixed mineral powders were ground under ethanol in an agate mortar and then dried overnight in an oven at 150 °C. Gold capsules measuring 1 cm × 3 mm × 0.2 mm were loaded with ~20 mg of rock powder and ~2 mg of distilled water. The capsules were welded, checked for weight loss, and then placed in an oven overnight at 150 °C to check for leaks. Successfully sealed capsules were then loaded into cold-seal Rene-41 reaction vessels with stainless-steel filler rods and pressurized at 200 MPa. The pressure medium was water plus trace amounts of a hydrocarbon-based rust inhibitor that imposed an f_{O_2} slightly less than the NNO buffer of the reaction vessel. Pressure was monitored by a factory-calibrated Heise Bourdon-tube gauge, and all experiments were conducted open to the gauge and a 2 L pressure buffer; pressure uncertainty is <1 MPa. Temperatures were monitored by internal Chromel-Alumel thermocouples; temperature uncertainty is ±2 °C. Experiments were quenched isobarically in an air jet to <300 °C in 10–50 s. Capsules were weighed after experiments to check for leaks; however, all capsules gained weight (~0.2 mg) owing to diffusion of Ni from the reaction vessel into the precious metal capsule. Experimental products were analyzed by optical examination, scanning and back-scattered electron (BSE) imaging, and energy- and wavelength-dispersive X-ray spectroscopy. Quantitative electron microprobe analyses of experimental products were exclusively performed using wavelength-dispersive X-ray techniques. Analytical conditions, including beam conditions, diffracting crystals used, counting times, and lower limits of detection (LLDs), are tabulated in the Appendix. Details of the SIMS analyses are also included in the Appendix.

We used two different approaches to experimental conditions. Preconditioned experiments were heated to 750

°C for 3 d and then cooled isobarically to experimental temperatures (reverse-direction expts.). Isobaric cooling to 650 °C consisted of either stepwise cooling in 50 °C intervals or cooling directly to the final experimental temperature in a single step. The rest of the experiments were heated directly to the temperature of interest (forward-direction expts.). We should emphasize, however, that the forward- and reverse-direction methods do not constitute a reversal of element partitioning. In both cases, the constituents present in starting materials dissolve into and then reprecipitate from melt. Experiments, both forward and reverse, were conducted on a 50 °C interval from 650 to 750 °C. Experiments at 750 °C were performed in the forward direction only.

Conditions of melting

To induce partial melting of the synthetic metapelite rock powders, we used previously determined phase relationships for simple granite systems (Fig. 1). The experiments were designed to generate large quantities of melt along the low-pressure (200 MPa) metastable extension of the reaction

$$\text{quartz} + \text{albite} + \text{muscovite} + H_2O = \text{melt} + \text{aluminum silicate} \quad (1)$$

(cf. Storre and Karotke, 1971). We had no difficulty working with the metastable extension of this reaction, which lies at approximately 625 °C and 200 MPa (Fig. 1). That is, Reaction 1 consumed all quartz before the subsolidus reaction

$$\text{quartz} + \text{muscovite} = \text{orthoclase} + \text{aluminum silicate} + H_2O \quad (2)$$

could proceed. The steep negative slope of Reaction 1 is important because it is nearly temperature-independent, allowing us to make reasonable extrapolations concerning anatexis of metapelites to higher pressures. Experiments were quartz undersaturated and muscovite oversaturated above the solidus; thus, the next heterogeneous reaction with increasing temperature involved the equilibrium

$$\text{muscovite} = \text{orthoclase} + \text{corundum} + H_2O \quad (3)$$

which was encountered near 715 °C, as reported by Yoder and Eugster (1955). This reaction is important because it represents the first appearance of alkali feldspar (nominally orthoclase) in aluminous metapelites at pressures above about 200 MPa (Fig. 1).

Approach to equilibrium

By monitoring the chemical and textural features of experimental products, we established that durations of 4 weeks were necessary for most experiments to attain textural and chemical steady state. Hexagonal crystal shapes (*c* axis perpendicular to view) or sharply bounded prismatic laths (*c* axis parallel to view) of biotite and muscovite indicated that the original micas reacted with melt to produce new micas (Fig. 2). Euhedral, unzoned micas indicated a close approach to equilibrium with melt. Remnant, unreacted biotite is rarely present as cores (higher BSE intensity as a result of higher Cs and Rb contents) overgrown by new biotite rims (lower BSE intensity). White mica (muscovite) is present in forward-direction 650–700 °C experiments as both recrystallized and unreacted grains. Reverse-direction experiments to 650 °C contain recrystallized, euhedral white mica exclusively. Unreacted white mica is manifested by an irregular embayed interface with melt and is thus easily distinguished from its recrystallized counterpart. Only euhedral, prismatic laths of biotite and muscovite were analyzed in this study.

From BSE signals, recrystallized biotite and muscovite appear to be extremely homogeneous. This is fortunate because the small grain size of crystal cross sections precluded very selective or multiple analyses of individual grains. Micas selected for EMPA were oriented such that their [100] zonal planes were nearly parallel to the incident beam. This orientation gave the greatest exposed thickness of mica through which the beam did not penetrate to glass. Generally, biotite and white mica from duplicate experiments show close compositional similar-

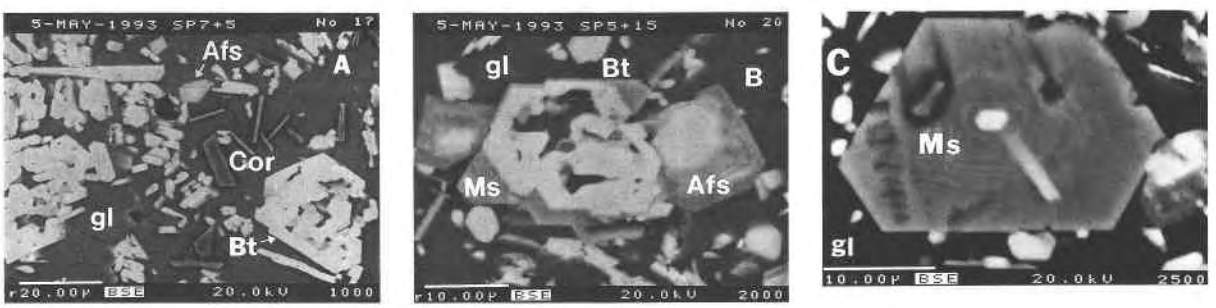

Fig. 2. Back-scattered electron (BSE) images of biotite, muscovite, feldspar, corundum, and glass. (**A**) Euhedral biotite (Bt), alkali feldspar (Afs), and corundum (Cor) in melt (gl) from SP7+5 (700 °C, reversed). High BSE intensity of biotite is due to high concentrations of Ba, Rb, and Cs; high BSE intensity of corundum is due to high concentrations of Ti and Fe. (**B**) Euhedral biotite crystals overgrown by white mica (Ms) in SP5+15 (650 °C, reversed). (**C**) Close-up of a euhedral white mica crystal in SP5+15. Inclusions are biotite and spinel. The variation in BSE contrast in the white mica is the result of slight charging effects caused by spalling of the mica during polishing, not compositional zoning.

TABLE 3. Glass compositions

	4 − 2 650 F *n* = 72	4 − 6 650 R *n* = 12	4 − 3 700 F *n* = 42	4 − 8 750 F *n* = 10	6 + 6 650 R *n* = 40	6 + 5 700 R *n* = 22	6 + 3 700 R *n* = 20	6 + 7 700 F *n* = 38	6 + 4 750 F *n* = 45
SiO_2	67.51(0.12)	66.90(0.18)	67.75(0.08)	66.83(0.16)	63.73(0.13)	62.44(0.16)	61.36(0.11)	59.60(0.34)	59.94(0.13)
TiO_2	*0.04*	*0.04*	*0.04*		*0.04*	0.05(0.01)	0.06(0.00)	0.06(0.00)	0.09(0.00)
Al_2O_3	14.50(0.06)	15.07(0.18)	14.65(0.04)	15.19(0.13)	15.79(0.06)	17.07(0.05)	17.47(0.05)	16.58(0.06)	17.63(0.05)
MgO	0.15(0.00)	0.06(0.00)	0.08(0.00)		0.05(0.01)	0.07(0.00)	0.08(0.00)	0.07(0.00)	0.12(0.00)
CaO	0.11(0.02)	0.11(0.00)	0.11(0.00)	0.10(0.01)	0.47(0.01)	0.62(0.01)	0.67(0.01)	0.63(0.01)	0.76(0.01)
MnO	0.07(0.00)	0.09(0.00)	0.08(0.00)		0.05(0.00)	0.06(0.00)	0.06(0.00)	0.06(0.00)	0.07(0.00)
FeO	0.62(0.01)	0.42(0.12)	0.48(0.00)		0.40(0.01)	0.54(0.01)	0.64(0.04)	0.64(0.01)	0.85(0.01)
NiO	*0.04*		*0.04*		*0.04*	*0.04*		*0.04*	*0.04*
SrO	*0.07*	*0.07*	*0.07*		0.11(0.01)	0.32(0.03)	0.24(0.04)	0.19(0.01)	0.50(0.02)
BaO	*0.13*	*0.13*	*0.13*		0.11(0.01)	0.23(0.02)	0.22(0.01)	0.25(0.01)	0.45(0.01)
Na_2O	3.69(0.09)	2.94(0.03)	3.31(0.03)	3.41(0.05)	3.08(0.03)	3.44(0.04)	3.48(0.03)	3.18(0.04)	3.31(0.03)
K_2O	3.29(0.06)	4.53(0.03)	4.46(0.03)	4.88(0.07)	3.05(0.03)	3.36(0.03)	3.43(0.03)	3.10(0.04)	3.48(0.02)
Rb_2O	*0.05*	*0.05*	*0.05*		0.67(0.01)	0.62(0.00)	0.71(0.01)	0.62(0.00)	0.64(0.00)
Cs_2O	*0.11*	*0.11*	*0.11*		1.14(0.01)	0.95(0.01)	0.93(0.02)	0.95(0.00)	0.86(0.01)
F	0.69(0.02)	0.61(0.01)	0.73(0.03)		2.01(0.04)	2.03(0.03)	1.68(0.03)	2.18(0.07)	2.04(0.03)
Li_2O*		0.22							
P_2O_5	0.05(0.00)	0.03	0.05(0.00)		0.14(0.00)	0.13(0.00)	0.13(0.01)	0.13(0.00)	0.12(0.00)
Total	91.12	91.38	92.14		90.88	91.97	91.16	88.28	90.90
O = F	90.83	91.12	91.83		90.03	91.12	90.45	87.36	90.04
ASI	1.49	1.43	1.41	1.38	1.64	1.58	1.60	1.66	1.61
Femic	0.81	0.61	0.54		0.54	0.72	0.84	0.83	1.13
Mg′	0.28	0.20	0.20		0.17	0.17	0.17	0.15	0.19
					CIPW norm				
Q	38	36	35	31	38	32	30	33	29
Ab	35	28	31	32	33	37	37	35	37
Ms	21	23	18	18	28	27	29	30	29
Or	6	13	16	18	2	4	4	1	5
C	0	0	0	0	0	0	0	0	0

Note: Italics = detection level; blank = not determined; R = reverse experiment; F = forward experiment; Mg′ = Mg/(Mg + Fe + Mn); ASI = molar Al/Σ alkalis + Ca, Ba, and Sr; femic = TiO_2 + MgO + FeO + MnO; standard deviation shown in parentheses (see Appendix).
* Li_2O by SIMS probe.

ities that suggest to us that our experiments are reproducible.

RESULTS

Partial melting of Synpel 4 from 625 to 750 °C produced melt (quenched to glass) and muscovite ± corundum ± mullite or other aluminum silicate ± spinel ± feldspar ± biotite. Phase assemblages in Synpel 5, 6, 7, and 8 are more complicated, with biotite, muscovite, feldspar, and melt present in lower temperature (650–700 °C), forward-direction experiments, and biotite, feldspar, corundum, and glass ± spinel present in 750 and 700 °C reverse-direction experiments. Melt is present in 625 and 650 °C forward-direction experiments but is absent at 600 °C, thus bracketing the solidus of the system between 600 and 625 °C. At 700 °C, melt makes up at least 50% of the charge by volume, with crystals well distributed within the glass. Melt is the dominant phase in 750 °C forward-direction experiments.

Above the minimum melting temperature, where one (quartz) or more phases disappear by melting, the next heterogeneous reaction that is observed with increasing T is the terminal reaction for muscovite (muscovite = orthoclase + corundum + H_2O), where orthoclase becomes a component of alkali feldspar. Muscovite disappears from forward experiments at 725 °C but crystallizes in reversed experiments at 700 and 650 °C and 200 MPa (H_2O). Though not discussed here, feldspars tend to be zoned, especially in experiments in which Ba and Sr were added (Fig. 2). Corundum forms thin euhedral hexagonal plates, and as the gradual melting of biotite proceeds, the corundum gains a substantial component of sapphire (Fe + Ti), which appears brighter in BSE intensity than the pure alumina phase (e.g., Fig. 2).

Melt

Compositions of glasses (representing quenched melts), determined by EMPA, are presented in Table 3. Experiments SP4-6, SP5-11, SP7+10, and SM-7 were analyzed by SIMS methods in addition to EMPA, and the analyses are given in Table 4. Above the minimum melting temperature of the system, variations in melt composition follow trajectories determined by the melting of remnant phases (muscovite, biotite, or albite present in excess above the proportions at the minimum). In terms of the major phases added, the normative composition (weight percent) of the minimum melt is near $Ab_{30}Or_{15}Ms_{20}Qtz_{35}$ or $Ab_{30}Or_{30}Cor_6Qtz_{34}$ (Table 3). In general, glasses are highly silicic (>70 wt% SiO_2 on an anhydrous basis), with SiO_2 decreasing with increasing temperature (Fig. 3A). Al is strongly concentrated in these melts (14.5–17.9 wt% Al_2O_3) and increases with temperature (Fig. 3B) despite the presence of at least one peraluminous phase (corundum, aluminum silicate, mullite, spinel, biotite, or muscovite) at all temperatures in every experiment. However, apparent Al saturation indices [(ASI) molar $Al_2O_3/\Sigma\ Na_2O$,

TABLE 3.—*Continued*

	5 + 15 650, R *n* = 20	5 + 14 650, R *n* = 10	5 + 8 650, R *n* = 15	5 + 7 700, R *n* = 13	5 + 5 700, F *n* = 18	5 + 11 700, R *n* = 25	5 + 9 700, F *n* = 10	5 + 6 750, F *n* = 12	5 − 11 750, F *n* = 12
SiO_2	63.94(0.20)	64.27(0.25)	65.90(0.17)	63.52(0.24)	64.04(0.12)	62.58(0.27)	63.49(0.19)	61.07(0.10)	62.14(0.14)
TiO_2	0.09(0.01)	0.07(0.01)	0.06(0.01)	0.07(0.02)	0.05(0.00)	0.08(0.02)	0.09(0.02)	0.08(0.01)	0.11(0.01)
Al_2O_3	15.84(0.08)	15.67(0.14)	15.61(0.10)	16.93(0.06)	17.00(0.04)	16.51(0.11)	16.58(0.07)	17.59(0.05)	17.28(0.05)
MgO	0.16(0.02)	0.11(0.02)	0.12(0.02)	0.13(0.04)	0.07(0.00)	0.20(0.07)	0.09(0.02)	0.10(0.00)	0.12(0.00)
CaO	0.83(0.01)	0.82(0.01)	0.80(0.02)	0.94(0.01)	1.01(0.01)	0.87(0.01)	0.89(0.02)	0.91(0.01)	1.07(0.02)
MnO	0.07(0.00)	0.07(0.00)	0.08(0.01)	0.06(0.01)	0.07(0.01)	0.07(0.00)	0.08(0.01)	0.08(0.01)	0.10(0.01)
FeO	0.74(0.06)	0.64(0.04)	0.61(0.05)	0.73(0.10)	0.61(0.01)	0.62(0.04)	0.67(0.04)	0.90(0.01)	0.90(0.01)
NiO	*0.04*	*0.04*	*0.04*	*0.04*	*0.04*	*0.04*	*0.04*	*0.04*	
SrO	0.45(0.04)	0.21(0.03)	0.22(0.02)	0.43(0.06)	0.40(0.02)	0.46(0.03)	0.41(0.03)	0.32(0.02)	*0.07*
BaO	0.27(0.03)	0.21(0.04)	0.22(0.02)	0.32(0.04)	0.27(0.01)	0.32(0.04)	0.29(0.02)	0.40(0.03)	*0.13*
Na_2O	1.95(0.02)	1.54(0.07)	2.19(0.02)	2.03(0.10)	2.32(0.01)	1.83(0.07)	1.97(0.07)	2.16(0.02)	2.45(0.04)
K_2O	3.28(0.04)	3.13(0.05)	3.29(0.04)	3.77(0.04)	3.86(0.02)	3.53(0.03)	3.46(0.04)	4.20(0.01)	4.42(0.05)
Rb_2O	0.59(0.01)	0.53(0.02)	0.60(0.01)	0.64(0.01)	0.68(0.01)	0.57(0.01)	0.56(0.01)	0.65(0.02)	0.60(0.01)
Cs_2O	1.04(0.02)	1.07(0.03)	1.09(0.03)	0.86(0.02)	0.96(0.01)	0.87(0.02)	0.90(0.03)	0.88(0.06)	0.85(0.02)
F	1.74(0.04)	1.79(0.07)	1.70(0.06)	1.95(0.15)	1.67(0.04)	1.61(0.03)	1.96(0.03)	2.06(0.01)	1.54(0.05)
Li_2O^+									0.75
P_2O_5	0.12(0.01)	0.12(0.01)	0.14(0.01)	0.12(0.01)	0.12(0.00)	0.12(0.01)	0.13(0.01)	0.11(0.01)	0.12(0.01)
Total	91.15	90.29	92.67	92.54	93.17	90.28	91.61	91.55	92.65
O = F	90.42	89.54	91.95	91.72	92.47	89.60	90.78	90.68	92.00
ASI	1.65	1.86	1.61	1.62	1.53	1.70	1.69	1.60	1.32
Femic	1.06	0.89	0.87	0.99	0.80	0.97	0.93	1.16	1.23
Mg′	0.26	0.22	0.24	0.23	0.15	0.34	0.18	0.15	0.19
					CIPW norm				
Q	46	49	44	36	38	40	40	36	33
Ab	25	17	26	28	27	26	27	26	26
Ms	27	33	28	26	27	31	32	31	29
Or	3	0	2	9	8	3	2	8	11
C	0	1	0	0	0	0	0	0	0

K_2O, Rb_2O, Cs_2O, CaO, BaO, and SrO] vary only between 1.5 and 1.8 because the K_2O content of melt also increases with temperature (Fig. 3C). The concentration of Li in glass from select Synpel experiments, determined by SIMS, is ~3500 ppmw (or 0.75 wt% Li_2O) for both high- (750 °C; SP5-11) and low-temperature (650 °C; SP7+10) experiments. The source of Li in these melts is both starting muscovite and biotite. Concentrations of Li in an experiment (SP4-6) without the starting biotite is ~1000 ppmw; the source of Li in this case is the starting muscovite. When Li is accounted for (e.g., SP7+10, SP5-11) the ASI of the melts drops to values of 1.3–1.4.

One consequence of the high concentration of Al_2O_3 with respect to alkalis is that the glasses typically contain >20 wt% of normative muscovite (the sum of normative orthoclase and corundum, Table 3). The glasses do, however, contain >10 wt% of normative orthoclase components, which indicates that muscovite melts incongruently, as reported by Storre and Karotke (1971). The lowest temperature melts (650 °C) project to $Ab_{27}Or_{23}Qtz_{50}$ on the metaluminous ternary (i.e., with excess Al removed; Fig. 4). On the quartz-albite-orthoclase (weight percent) diagram, the glasses show a progressive increase in orthoclase with increasing temperature, reflecting the progressive melting of muscovite or of alkali feldspars and biotite at high temperature.

Concentrations of the sum of the femic components (TiO_2, MgO, MnO, and FeO) are nearly always <1 wt% as oxides, so that the melts correspond to typical leucogranites. The femic sum in melt tends to increase with rising temperature primarily because of rising concentrations of FeO (Fig. 5A). FeO concentrations in melt and values of Mg′ [=Mg/(Mg + Mn + Fe)] in biotite both increase with temperature (Fig. 5B).

Concentrations of alkalis and alkaline earths vary in proportion to the melting reactions involving phases that survive above the minimum. For example, melts of Synpel 6, which contain more albite, become increasingly sodic with increasing T as albite continues to melt. A general increase in the K content of melt, however, corresponds to the progressive reaction of biotite to melt components plus spinel or the Fe-Ti (sapphire) component of corundum and derives an additional component from the melting of alkali feldspar (which is produced in abundance with the breakdown of excess muscovite above 725 °C). Ca was unintentionally added to the bulk compositions by impurities in the biotite separates (as plagioclase); concentrations of CaO vary between 0.4 and 1.2 wt% in Synpel 5, 6, 7, and 8 glasses. Synpel 4, which does not have biotite in the starting assemblage, contains ~0.1 wt% CaO.

Cs and Rb behave quite differently in the Synpel system, as shown in Figure 6A and 6B. Concentrations of Rb_2O in melt increase or remain constant, whereas Cs_2O decreases with increasing temperature. BaO concentrations increase with increasing temperature (Fig. 6C). The

TABLE 3.—*Continued*

	7 + 10 650, R *n* = 20	7 + 6 650, R *n* = 20	7 + 5 700, R *n* = 15	7 + 7 700, F *n* = 12	7 + 4 750, F *n* = 20	8 + 5 700, F *n* = 7	8 + 7 750, F *n* = 36	8 + 2 750, F *n* = 40	SM-7 660, R *n* = 19
SiO_2	65.40(0.25)	64.20(0.12)	62.60(0.15)	61.86(0.16)	60.66(0.14)	62.05(0.97)	63.60(0.45)	64.37(0.14)	69.60(0.17)
TiO_2	0.07(0.01)	0.06(0.01)	0.07(0.01)	0.06(0.01)	0.09(0.01)	0.05(0.06)	0.08(0.03)	0.11(0.01)	*0.04*
Al_2O_3	15.88(0.13)	16.37(0.12)	17.09(0.05)	17.28(0.04)	18.48(0.05)	16.19(0.23)	16.57(0.27)	16.44(0.05)	13.78(0.08)
MgO	0.08(0.02)	0.08(0.01)	0.11(0.01)	0.08(0.01)	0.10(0.01)	0.17(0.13)	0.10(0.02)	0.14(0.01)	*0.02*
CaO	0.87(0.01)	0.96(0.01)	1.15(0.01)	0.98(0.01)	1.02(0.01)	0.56(0.04)	0.50(0.04)	0.48(0.01)	0.38(0.01)
MnO	0.06(0.00)	0.07(0.00)	0.08(0.01)	0.08(0.01)	0.09(0.00)	0.09(0.03)	0.08(0.02)	0.08(0.00)	0.04(0.01)
FeO	0.53(0.06)	0.53(0.03)	0.67(0.03)	0.67(0.02)	0.84(0.04)	0.88(0.44)	0.66(0.06)	0.61(0.04)	0.47(0.01)
NiO	*0.04*	*0.04*	*0.04*	*0.04*	*0.04*	*0.04*	*0.03*	*0.04*	*0.04*
SrO	*0.07*	0.20(0.02)	0.24(0.02)	0.39(0.03)	0.65(0.03)	0.38(0.10)	0.26(0.10)	0.16(0.03)	*0.07*
BaO	*0.13*	0.15(0.03)	0.21(0.01)	0.19(0.03)	0.28(0.02)	0.27(0.09)	0.38(0.06)	0.40(0.02)	*0.13*
Na_2O	1.87(0.09)	1.84(0.04)	2.08(0.02)	1.83(0.03)	1.72(0.07)	2.40(0.13)	2.80(0.12)	2.61(0.07)	3.91(0.03)
K_2O	3.95(0.08)	3.50(0.06)	4.21(0.03)	3.79(0.02)	4.90(0.05)	3.34(0.15)	4.44(0.08)	4.82(0.05)	4.75(0.02)
Rb_2O	0.55(0.01)	0.59(0.01)	0.62(0.01)	0.61(0.01)	0.68(0.01)	0.35(0.03)	0.33(0.03)	0.36(0.01)	0.06(0.01)
Cs_2O	1.10(0.02)	1.24(0.02)	1.03(0.02)	1.09(0.02)	0.93(0.02)	0.45(0.06)	0.40(0.06)	0.38(0.02)	*0.11*
F	1.86(0.08)	1.92(0.04)	2.17(0.04)	2.13(0.04)	2.39(0.03)	0.75(0.04)	1.02(0.07)	1.08(0.03)	1.59(0.09)
Li_2O^+	0.77								
P_2O_5	0.09(0.01)	0.09(0.01)	0.13(0.01)	0.16(0.01)	0.14(0.00)	0.09(0.02)	0.07(0.02)	0.08(0.00)	
Total	93.32	91.84	92.50	91.24	93.01	88.06	91.32	92.16	94.99
O = F	92.54	91.03	91.59	90.34	92.00	87.74	90.89	91.71	94.32
ASI	1.65	1.70	1.53	1.71	1.60	1.89	1.60	1.62	1.12
Femic	0.74	0.74	0.93	0.89	1.12	1.19	0.92	0.94	0.51
Mg′	0.19	0.19	0.21	0.16	0.16	0.24	0.20	0.26	1.00
					CIPW norm				
Q	40	44	37	39	32	39	33	31	31
Ab	25	23	25	23	24	30	31	30	37
Ms	27	31	33	34	32	27	24	24	7
Or	8	2	6	4	13	4	12	14	26
C	0	0	0	0	0	0	0	0	0

relatively high concentrations of these oxides, especially Cs_2O (0.8–1.3 wt%) and Rb_2O (0.6–0.7 wt%), stem only from their high initial contents in the starting biotite from the Tanco pegmatite. The crystal-melt partition coefficients (discussed below) are more meaningful than the absolute concentrations of these elements.

Concentrations of LILEs at trace levels (Li, Rb, Cs, Sr, and Ba) in one Synpel 4 experiment (SP4-6) and one Spor Mountain experiment (SM-7), determined by SIMS, are tabulated in Table 4. Concentrations of these elements are very low (1500–5 ppmw), corresponding to dilute components.

F concentrations are very high in all Synpel melts. In Synpel 4, the concentration of F in a 650 °C forward-direction experiment is ~0.7 wt% and is due solely to the breakdown of muscovite. In Synpel experiments 5–7, wherein both muscovite and biotite contribute F to melt, concentrations of F vary between 1.6 and 2.2 wt%. Concentrations of F in these melts are also temperature dependent, as shown by Figure 7A, with the F content of melt increasing with T. This is an interesting observation because F remains constant or decreases with temperature in biotite (Fig. 7B), as required by mass balance. Other compositional characteristics of biotite are discussed below.

TABLE 4. SIMS probe analyses of glass

Experiment	4-6	5-11	SM-7	7 + 10
Li	1013	3500	98	3594
Rb	781	6857	1501	6068
Sr	101	184	72	147
Cs	70	9224	115	11632
Ba	102	125	5	78

Note: Values are parts per million by weight.

Biotite

Biotite is present as euhedral hexagons and laths (Fig. 2) that are interpreted to represent starting biotite that reacted with melt to produce new biotite. Biotite crystals appear homogeneous by BSE imaging. In a few cases, remnants of the starting biotite, rimmed by new biotite, are present and are easily distinguished from new biotite by the bright BSE images of the former owing to their higher concentrations of Cs and Rb. Compositions of euhedral laths of biotite that have clearly crystallized from melt are presented in Table 5. SIMS analyses of four samples are given in Table 6. The composition of biotite grown from melt (i.e., at equilibrium with melt) differs from that of the starting Tanco biotite (Table 1). The most significant changes are higher concentrations of TiO_2, Al_2O_3, FeO, BaO, and K_2O and lower SiO_2, Rb_2O, Cs_2O, and F in the recrystallized biotite. Cation site assignments for the recrystallized biotite are presented below.

Tetrahedral cations. Biotite analyses were recalculated on the basis of 24 (O, OH, and F). Experimentally grown biotite contains between ~5.3 and 5.7 atoms of Si per formula unit (p.f.u.). Tetrahedral Al, or $^{[4]}$Al, defined as the difference between 8.0 and the number of Si atoms, is between ~2.3 and 2.7 atoms p.f.u. The number of Si atoms per formula unit in biotite decreases while total Al increases slightly with rising temperature.

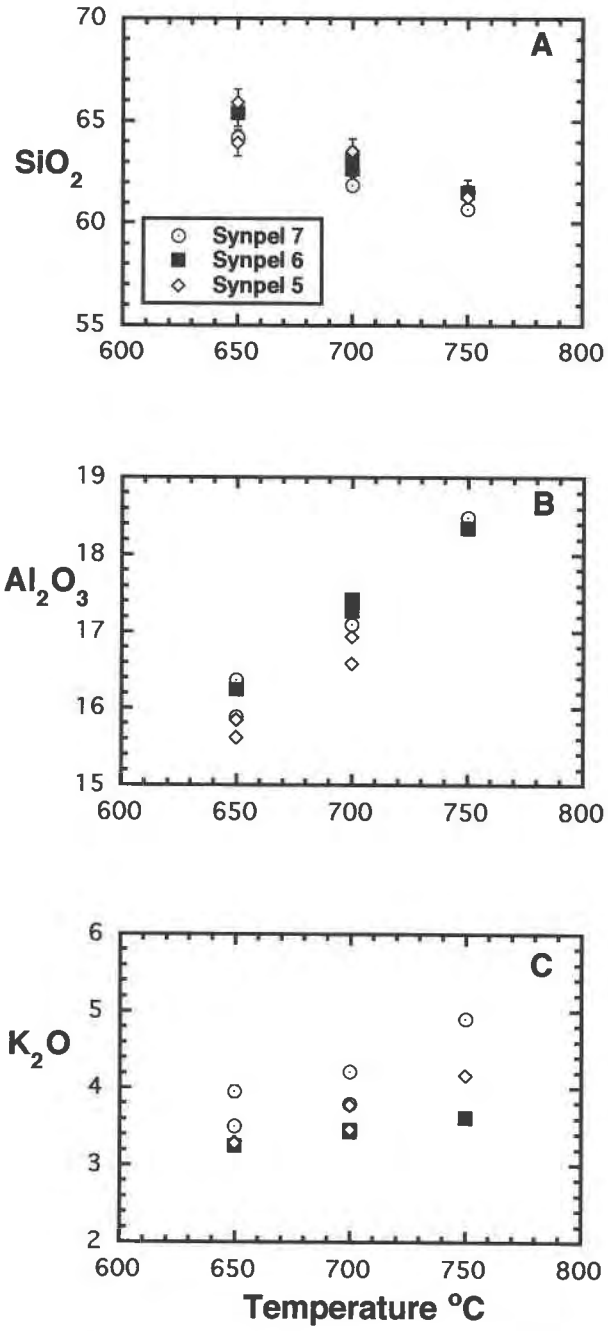

Fig. 3. Compositions of analyzed glasses (quenched melt) in the experimental charges. Symbols are as follows: diamonds = Synpel 5, squares = Synpel 6, circles = Synpel 7. Error bars represent 1σ errors, as described in the Appendix. (**A**) SiO_2 vs. temperature. Silica is highest at low temperature where quartz is lost from the starting assemblage. (**B**) Al_2O_3 vs. temperature. Melting of white mica and continuous reaction of biotite with melt both contribute Al to melt. (**C**) K_2O vs. temperature. The rise in Al with temperature, as seen in **B**, is offset by a concomitant rise in K that keeps the ASI $\leq$ 1.4.

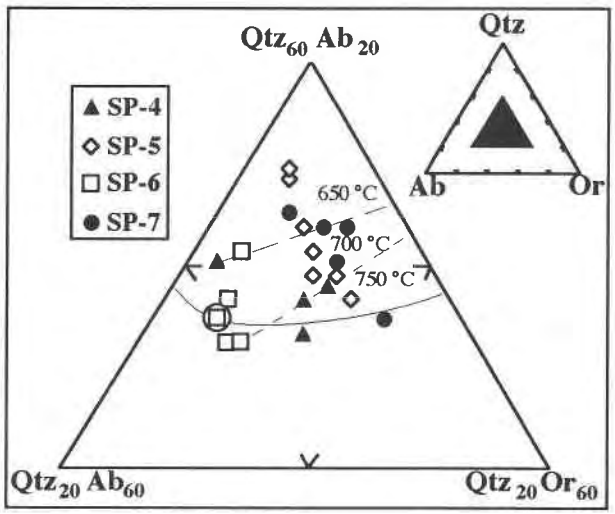

Fig. 4. Synpel melt compositions projected onto the metaluminous ternary quartz-albite-orthoclase. The 200 MPa H_2O-saturated minimum, approximately $Qtz_{35}Ab_{30}Or_{35}$ (open circle), and the quartz-alkali feldspar cotectic (solid line) were determined by Tuttle and Bowen (1958). Symbols are as follows: solid triangles = Synpel 4, diamonds = Synpel 5, squares = Synpel 6, solid circles = Synpel 7. Note that the projected melt compositions move progressively toward the orthoclase apex with increasing temperature (dashed lines = temperature contours), reflecting increasing muscovite and biotite melting.

Octahedral cations. Octahedral Al, defined as the difference between Al_{tot} and $^{[4]}Al$ (see above), is between ~1.2 and 1.8 atoms p.f.u. Figure 7C, a plot of $^{[6]}Al$ vs. Mg′, shows that biotite contains a significant siderophyllite component. There is, however, no systematic variation of $^{[6]}Al$ with the ASI of the melt. Li_2O concentrations in biotite vary with respect to temperature. Biotite from SP7+10 (650 °C, reversed) contains ~5900 ppmw Li (1.27 wt%), whereas biotite in SP5-11 (750 °C, forward) contains ~3500 ppmw Li (0.76 wt%). These Li concentrations correspond to up to 0.75 atoms p.f.u., which explains, in part, the low cation totals in biotite for which Li was not determined. TiO_2 concentrations are high (~1.4–2.1 wt% for up to 0.25 atoms p.f.u.) and increase with temperature (Fig. 8A). The majority of the octahedral sites, however, are filled by Fe (~1.8–2.1 atoms p.f.u.; all Fe is treated as FeO) and Mg (~1.3–1.9 atoms p.f.u.). Concentrations of MnO are typically low (<0.4 wt%), as are NiO concentrations (<0.04 wt%), but in a few cases the latter may reach concentrations as high as 0.5 wt%.

Interlayer cations. Concentrations of the alkaline earths CaO and SrO are all near or below their respective lower limits of detection. In contrast, Cs_2O, Rb_2O, BaO, Na_2O, and K_2O are all well above detection level. Concentrations of Cs_2O and Rb_2O show some variability, but no clear trend of increase or decrease emerges when plotted against temperature. BaO appears to increase in concentration with increasing temperature and correlates positively with TiO_2 (Fig. 8B).

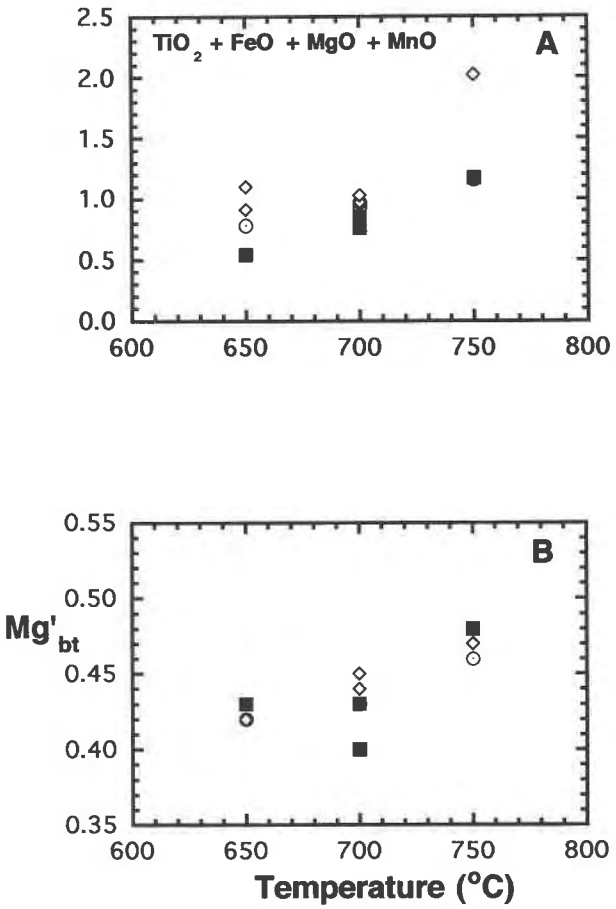

Fig. 5. (A) Femic components (FeO_{tot} + TiO_2 + MgO + MnO) vs. temperature in analyzed Synpel glasses. (B) Mg' [MgO/(Fe + MgO + MnO)] vs. temperature for experimentally grown Synpel biotites. Symbols as in Fig. 3A.

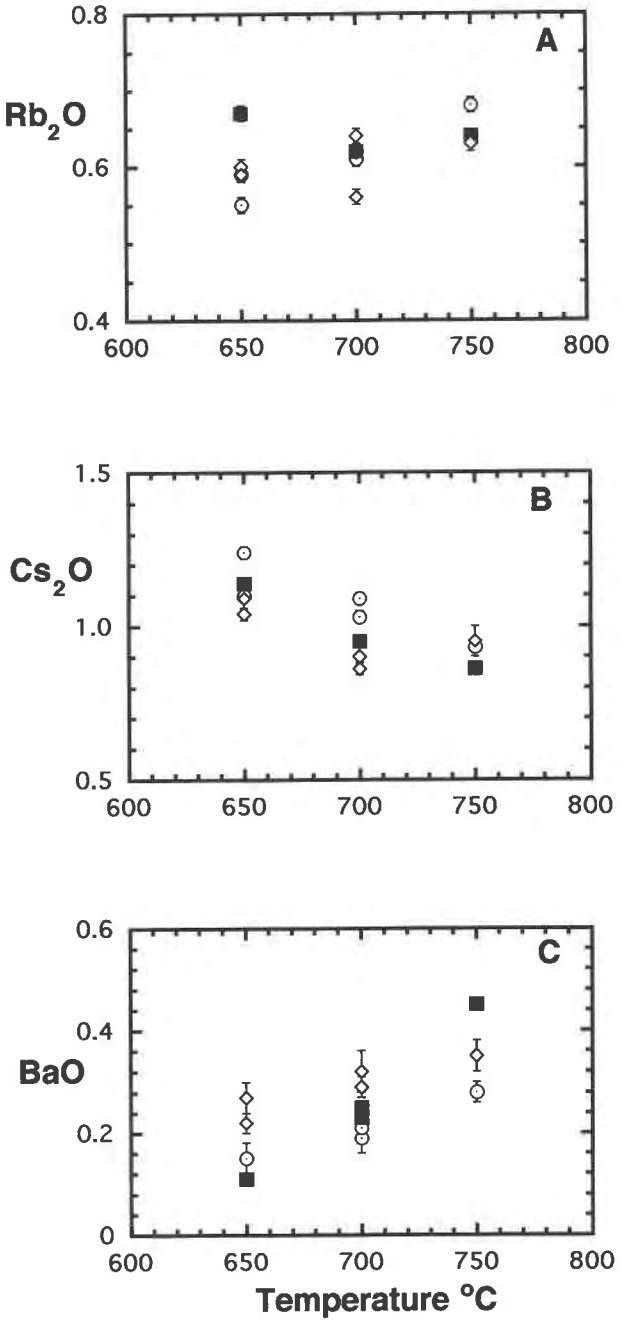

Fig. 6. Concentrations of the rare alkalis Rb, Cs, and Ba in Synpel experiments. Note that the presence of both Rb and Cs in melt is due to the reaction of biotite, the sole reservoir of rare alkalis in the starting assemblage, with melt. (A) Rb_2O vs. temperature. (B) Cs_2O vs. temperature. (C) BaO vs. temperature for Synpel glasses. Error bars represent 1σ errors. Symbols as in Fig. 3A.

Links between Ba and Ti substitution in biotite have been the subject of several papers. Mansker et al. (1979) proposed the substitution scheme

$$K + 3(Mg,Fe) + 3Si = Ba + 2Ti + 3Al + {}^{[6]}\square \quad (4)$$

to account for unusually high concentrations of BaO (up to 20 wt%) in micas from nephelinites. In contrast, Guo and Green (1990) suggested the substitution

$$2K + 4(Mg,Fe) + 4Si = Ba + 3Ti + 4Al + {}^{[6,12]}\square \quad (5)$$

to account for high concentrations of BaO and TiO_2 in experimentally produced biotite in a lamproititic composition.

Compositions of Synpel biotite (Table 5) indicate that neither of the above substitution schemes is appropriate (Ba:Ti = 1:1) for these compositions. Rather, a simple exchange,

$$^{[12]}K + {}^{[4]}Si = {}^{[12]}Ba + {}^{[4]}Al \quad (6)$$

appears to be the dominant substitution mechanism for both biotite and white mica, as observed for 1 *M* trioctahedral polytypes (Brigatti and Poppi, 1993). When other interlayer cations (Na, Rb, and Cs) are considered, the correlation between interlayer and tetrahedral layer site occupancies is improved (Fig. 9A). The simultaneous rise in Ti and Ba with temperature may be an artifact of two concomitant, although unrelated, exchange reactions. The

proposed mechanism for Ba involves Ba-K exchange in the interlayer site coupled with Si-Al exchange in the tetrahedral site, as discussed above. Ti may enter biotite octahedral sites by the Ti-Tschermak exchange mechanism, as previously suggested by Dymek (1983):

$$^{[6]}Ti^{4+} + {}^{[6]}(Mg,Fe,Mn)^{2+} = 2^{[6]}Al^{3+}. \quad (7)$$

This exchange is illustrated for both Synpel biotite and white mica in Figure 9B. A reference line with a slope of −1 passes through both sets of data in accord with this mechanism.

Concentrations of Na_2O exceed 0.5 wt% in many of the analyzed biotite crystals, but K_2O, up to and exceeding 1.5 atoms p.f.u., is clearly the dominant cation in the interlayer site.

OH site. Concentrations of F in biotite appear to remain constant or decrease slightly with increasing temperature (Fig. 7B). These data disagree with previous work that shows F increasing strongly with increasing temperature (Patiño Douce and Johnston, 1991). Reconnaissance electron microprobe analyses to determine Cl concentrations found that they are below detection limits.

White mica

White mica is present in forward-direction experiments to 650 and 700 °C and in 650 °C reverse-direction experiments. White micas in the latter experiments are manifested as euhedral laths or hexagonal plates that show no visible compositional zoning as determined by BSE imaging (Fig. 2). In contrast, white micas observed in the forward-direction experiments are anhedral to subhedral in habit with irregular, embayed boundaries with melt. We interpret white micas from the reverse-direction experiments as crystals precipitated from melt, whereas those from forward-direction experiments represent remnant, incompletely reacted material.

Tetrahedral cations. Experimentally grown white mica contains between ~6.2 and 6.6 atoms of Si p.f.u. Tetrahedral Al, defined as the difference between 8.0 and the number of Si atoms, is between ~1.4 and 1.8 atoms p.f.u.

Octahedral cations. Octahedral Al, defined as the difference between Al_{tot} and $^{[4]}Al$ (see above), is between ~3.3 and 3.6 atoms p.f.u., indicating that the octahedral site is filled predominately with Al. Concentrations of MgO and FeO show little variation (1.2–1.8 and 2.0–3.7 wt%, respectively) and collectively translate to approximately two-thirds of an atom. Small amounts of Mn and Ti (≤0.06 atoms p.f.u.) are also present. Mg′ for white mica varies from 0.44 to 0.50, which is greater than Mg′ in coexisting biotite.

Laths of white mica were generally too narrow for accurate SIMS analyses. A single point on one mica in SP4-6 gave 830 ppmw Li, whereas coexisting biotite contains 813 ppmw. Partition coefficients for Li and Rb between biotite and glass are anomalously low in comparison with other experiments (see below). Because of difficulties locating the SIMS ion beam on small targets and intimate nature of muscovite-biotite intergrowths and overgrowths in these experiments (Fig. 2), Li values for both muscovite and biotite in SP4-6 cannot be confirmed.

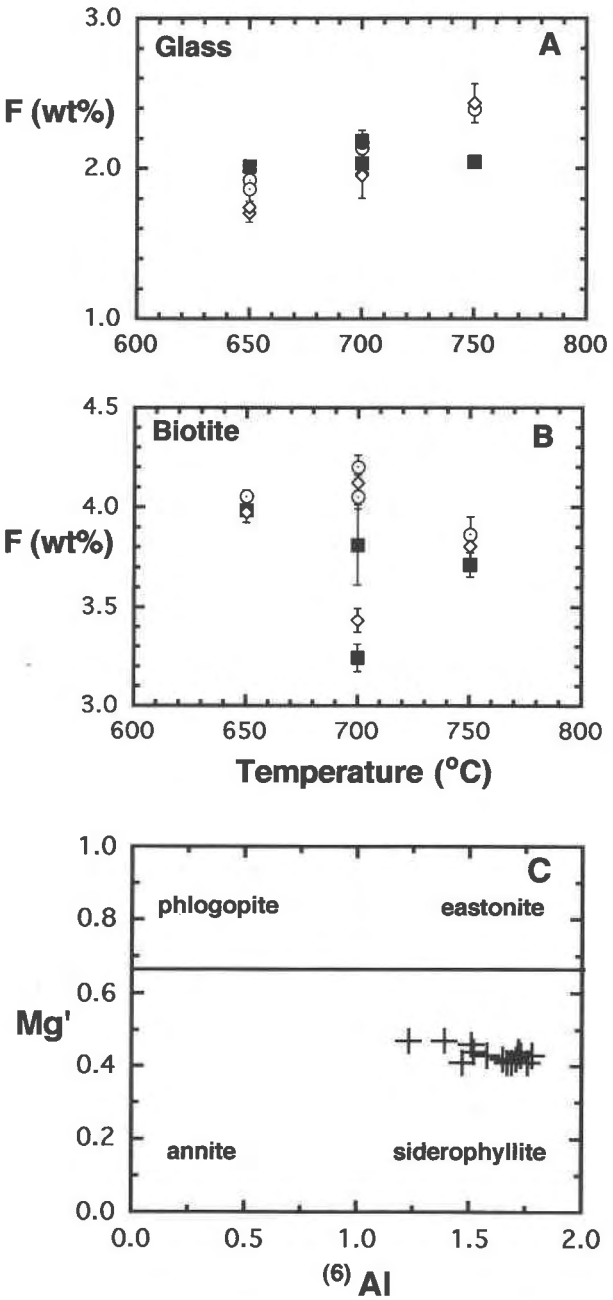

Fig. 7. (A) F (in weight percent) vs. temperature for Synpel glasses. Both white mica and biotite contribute F to melt. (B) Concentration of F in Synpel biotites. (C) Compositions of experimentally recrystallized biotites in terms of the end-members annite-siderophyllite-phlogopite-eastonite. Symbols as in Fig. 3A.

Interlayer cations. The interlayer site in white mica is filled predominately by K (1.4–1.7 atoms) and lesser amounts of Na (0.1–0.2 atoms p.f.u.). In experiments in which gels of celsian ($BaAl_2Si_2O_8$) and slawsonite ($SrAl_2Si_2O_8$) compositions were added, white micas contain measurable concentrations of BaO (~1 wt%) and SrO (up

TABLE 5. Compositions of biotite and white mica

wt% oxides	6 + 6 650 R $n = 5$	6 + 7 700 F $n = 4$	6 + 5 700 R $n = 10$	6 + 4 750 F $n = 10$	5 + 15 650 R $n = 10$	5 + 14 650 R $n = 11$	5 + 8 650 R $n = 14$
				Biotite			
SiO_2	36.78(0.27)	37.77(0.40)	34.65(0.38)	33.81(0.30)	36.46(0.17)	36.97(0.29)	37.17(0.45)
TiO_2	1.93(0.09)	1.65(0.08)	2.00(0.03)	2.06(0.15)	1.72(0.07)	1.56(0.03)	1.64(0.06)
Al_2O_3	22.80(0.16)	22.80(0.09)	22.18(0.08)	21.07(0.09)	22.52(0.11)	22.36(0.08)	21.53(0.20)
MgO	6.65(0.11)	6.00(0.02)	5.90(0.16)	8.08(0.06)	6.02(0.06)	6.00(0.08)	6.05(0.16)
CaO	0.02(0.01)	0.05(0.01)	0.02(0.01)	0.02(0.01)	0.04(0.00)	0.04(0.01)	0.05(0.02)
MnO	0.38(0.01)	0.27(0.01)	0.33(0.02)	0.26(0.01)	0.38(0.01)	0.34(0.01)	0.34(0.01)
FeO	15.31(0.19)	14.20(0.08)	15.10(0.26)	15.66(0.15)	14.94(0.10)	14.95(0.11)	14.45(0.19)
NiO	*0.04*	0.57(0.05)	2.25(0.13)	0.16(0.01)	*0.04*	*0.04*	0.30(0.04)
SrO	*0.07*	*0.07*	*0.07*	*0.07*	*0.07*	0.08(0.04)	*0.07*
BaO	3.15(0.12)	2.28(0.25)	2.60(0.13)	3.61(0.14)	3.42(0.11)	3.29(0.12)	2.76(0.24)
Na_2O	0.47(0.01)	0.55(0.01)	0.45(0.01)	0.41(0.01)	0.35(0.01)	0.36(0.01)	0.35(0.05)
K_2O	7.34(0.04)	7.52(0.08)	7.45(0.01)	7.15(0.05)	7.41(0.03)	7.40(0.05)	7.43(0.12)
Rb_2O	1.27(0.05)	1.27(0.07)	1.22(0.01)	1.17(0.03)	1.03(0.04)	1.03(0.04)	1.10(0.09)
Cs_2O	0.32(0.03)	0.33(0.06)	0.36(0.04)	0.31(0.03)	0.29(0.03)	0.30(0.04)	0.53(0.18)
H_2O	1.94(0.02)	2.03(0.09)	2.19(0.04)	1.91(0.04)	1.82(0.03)	1.77(0.03)	1.85
F	3.98(0.06)	3.81(0.20)	3.24(0.07)	3.71(0.06)	4.06(0.06)	4.18(0.05)	3.97(0.05)
Li_2O							
Total	102.45	101.13	99.96	99.57	100.50	100.69	99.62
O = F	100.77	99.52	98.59	98.01	98.80	98.96	97.95
				Cations			
Si	5.53	5.69	5.40	5.32	5.59	5.66	5.73
$^{(4)}Al$	2.47	2.31	2.60	2.68	2.41	2.34	2.27
$^{(6)}Al$	1.58	1.73	1.47	1.23	1.67	1.69	1.65
Li							
Ti	0.22	0.19	0.23	0.24	0.20	0.18	0.19
Mg	1.49	1.35	1.37	1.89	1.38	1.37	1.39
Mn	0.04	0.03	0.04	0.03	0.04	0.04	0.04
Fe	1.93	1.79	1.97	2.06	1.92	1.91	1.86
Ni	0.01	0.07	0.28	0.02	0.00	0.00	0.04
Ca	0.00	0.01	0.00	0.00	0.01	0.01	0.01
Sr	0.00	0.00	0.00	0.00	0.00	0.00	0.00
Ba	0.19	0.13	0.16	0.22	0.21	0.20	0.17
Na	0.14	0.16	0.14	0.13	0.10	0.11	0.10
K	1.41	1.44	1.48	1.44	1.45	1.44	1.46
Rb	0.12	0.12	0.12	0.12	0.10	0.10	0.11
Cs	0.02	0.02	0.02	0.02	0.02	0.02	0.03
OH	1.95	2.04	2.27	2.00	1.86	1.81	1.90
F	1.89	1.81	1.60	1.85	1.97	2.02	1.94
Total	15.16	15.04	15.29	15.40	15.10	15.07	15.05
Mg′	0.43	0.43	0.41	0.47	0.41	0.41	0.42

Note: H_2O estimated by site occupancy; F = forward-direction experiment; R = reverse-direction experiment; cations on the basis of 24 (OH,F); Li_2O by SIMS analyses; Mg′ = Mg/(Mg + Mn + Fe^{2+}); italics = detection limit; blank = not determined.

to 0.2 wt%). All analyzed white micas also contain moderate amounts of Rb_2O (~1 wt%) and Cs_2O (~0.2 wt%).

OH site. Concentrations of F in white mica are >3 wt% (except for experiment 8+6; Table 5). These concentrations correspond to approximately one-half of the total OH site. Reconnaissance electron microprobe analyses to determine Cl concentrations found that they are below detection limits.

The above discussion makes clear that white micas are predominately muscovite [i.e., $KAl_2(AlSi_3O_{10})(OH,F)_2$] with minor amounts of paragonite (Na_2O < 0.7 wt%) and titanium celadonite or phengite (TiO_2 < 0.6, MgO < 1.8, FeO < 3.7 wt%) components (Table 5).

PARTITION COEFFICIENTS AMONG BIOTITE, MUSCOVITE, AND MELT

Empirical partition coefficients are expressed as the weight concentration of the element of interest in biotite or muscovite divided by its concentration in glass. Following the recommendations of Beattie et al. (1993), these concentration ratios are denoted as $D(M)^{Bt/gl}$ and $D(M)^{Ms/gl}$ where D, Bt, Ms, gl, and M represent the partition coefficient, biotite, white mica, glass, and the trace element of interest, respectively. Partition coefficients determined in this study are listed in Table 7.

Ti, Mg, Mn, Fe, and Ni

The transition metals and Mg all partition strongly into biotite over melt. Average partition coefficients for TiO_2, MgO, and FeO are ~20, 50, and 20, respectively. Because NiO concentrations in glass are below detection, the concentration of NiO in biotite is divided by the calculated lower level of detection (see the Appendix) to yield minimum partition coefficient values. Partitioning of Mn between biotite and melt has a range of values between 3.2 and 5.5 but with most ratios between 3 and 4.

TABLE 5.—*Continued*

wt% oxides	5 + 9 700 F $n = 10$	5 + 7 700 R $n = 13$	5 + 6 750 F $n = 12$	5 – 11 750 F $n = 3$	7 + 10 650 R $n = 10$	7 + 6 650 R $n = 10$	7 + 7 700 F $n = 15$
				Biotite			
SiO_2	36.36(0.29)	35.90(0.21)	35.52(0.24)	36.86	37.69(0.32)	35.90(0.33)	35.60(0.18)
TiO_2	1.59(0.04)	1.44(0.08)	1.90(0.07)	1.82	1.53(0.07)	1.47(0.05)	1.60(0.05)
Al_2O_3	22.61(0.08)	21.49(0.05)	21.81(0.08)	21.94	22.72(0.30)	22.76(0.14)	23.06(0.07)
MgO	6.19(0.06)	6.39(0.06)	7.60(0.07)	7.70	5.89(0.10)	6.10(0.12)	5.92(0.05)
CaO	*0.02*	*0.02*	0.03(0.01)	0.04	0.02(0.01)	0.03(0.01)	*0.02*
MnO	0.26(0.01)	0.31(0.01)	0.28(0.01)	0.27	0.41(0.02)	0.39(0.01)	0.30(0.01)
FeO	13.73(0.10)	14.42(0.13)	15.12(0.10)	15.37	15.08(0.21)	14.78(0.23)	13.90(0.12)
NiO	0.47(0.11)	1.90(0.13)	0.42(0.06)	0.15	*0.04*	0.08(0.03)	*0.04*
SrO	*0.07*	*0.07*	*0.07*	*0.07*	*0.07*	*0.07*	*0.07*
BaO	2.79(0.04)	2.55(0.21)	3.37(0.07)	0.13	0.15(0.03)	2.15(0.13)	2.27(0.06)
Na_2O	0.33(0.01)	0.31(0.02)	0.33(0.01)	0.27	0.25(0.01)	0.20(0.01)	0.23(0.01)
K_2O	7.71(0.02)	7.67(0.10)	7.55(0.04)	8.68	8.83(0.08)	8.11(0.07)	7.97(0.04)
Rb_2O	1.18(0.03)	1.25(0.04)	1.07(0.03)	1.41	1.12(0.08)	1.04(0.06)	1.30(0.03)
Cs_2O	0.24(0.02)	0.33(0.03)	0.29(0.01)	0.41	0.34(0.07)	0.38(0.06)	0.35(0.04)
H_2O	1.77	2.13	1.96(0.03)	2.28	1.78	1.80	1.69
F	4.12(0.04)	3.37(0.06)	3.80(0.06)	3.31	4.25(0.06)	4.05(0.03)	4.20(0.06)
Li_2O				0.76	1.27		
Total	99.41	99.51	101.15	101.47	101.42	99.29	98.44
O = F	97.59	98.19	99.55	100.08	99.63	97.61	96.65
				Cations			
Si	5.61	5.58	5.45	5.51	5.70	5.55	5.55
$^{[4]}$Al	2.39	2.42	2.55	2.49	2.30	2.45	2.45
$^{[6]}$Al	1.72	1.52	1.39	1.37	1.76	1.71	1.78
Li				0.46	0.76		
Ti	0.18	0.17	0.22	0.20	0.17	0.17	0.19
Mg	1.42	1.48	1.74	1.71	1.33	1.41	1.37
Mn	0.03	0.03	0.03	0.03	0.04	0.04	0.03
Fe	1.77	1.87	1.94	1.92	1.91	1.91	1.81
Ni	0.06	0.24	0.05	0.02	0.00	0.01	0.00
Ca	0.00	0.00	0.00	0.00	0.00	0.00	0.00
Sr	0.00	0.00	0.00	0.00	0.00	0.00	0.00
Ba	0.17	0.16	0.20	0.00	0.01	0.13	0.14
Na	0.10	0.09	0.10	0.08	0.07	0.06	0.07
K	1.52	1.52	1.48	1.65	1.70	1.60	1.58
Rb	0.12	0.12	0.11	0.14	0.11	0.10	0.13
Cs	0.02	0.02	0.02	0.03	0.02	0.03	0.02
OH	1.82	2.21	2.01	2.27	1.80	1.86	1.76
F	2.01	1.66	1.84	1.56	2.03	1.98	2.07
Total	15.11	15.22	15.28	15.61	15.88	15.17	15.12
Mg′	0.44	0.44	0.47	0.47	0.41	0.42	0.43

Table 8 shows that TiO_2, MgO, and FeO are preferentially harbored by biotite over white mica. Partition coefficients for Mn between white mica and melt are ~1, and thus Mn is equally distributed between these two phases.

Li

The partition coefficient for Li between biotite and melt is 1.64 for SP7+10 (650 °C, reverse). This value is notably similar to the value obtained in SM-7 (1.67; 660 °C, reverse) despite the significant differences in melt and biotite compositions between the Synpel and Spor Mountain experiments. $D(Li)^{Bt/gl}$ for SP5-11 (750 °C, forward) is 1.01, implying that $D(Li)^{Bt/gl}$ decreases with increasing temperature. As noted above, results for SP4-6 (650 °C, reverse) do not follow these systematics; the value of $D(Li)^{Bt/gl}$ obtained on a single biotite analysis is 0.80. The estimated partition coefficient for Li between biotite and melt, therefore, lies between 1 and 2, with good evidence for temperature dependence awaiting further analyses.

The one SIMS analysis of Li in white mica (SP4-6; 650 °C) does not permit us to confirm the behavior of Li. Pending more definitive analyses, the partition coefficient for Li between Ms and melt $\approx$ 0.8, and that between Bt and Ms $\approx$ 1.

Ca, Sr, and Ba

Ca is partitioned into melt over biotite with values of $D(Ca)^{Bt/gl} \leq 0.08$, but it shows a slightly greater affinity for white mica [$D(Ca)^{Ms/gl} = 0.14$, 0.13, and 0.03]. Similar systematics are evident for the partitioning of Sr between micas and melt. Concentrations of Sr in biotite, determined by EMPA, are typically low and yield low (<0.4) partition coefficient values. Partition coefficients obtained by SIMS indicate consistently low (0.03–0.06) values of $D(Sr)^{Bt/gl}$. Sr concentrations in white micas, determined by EMPA, are higher than in biotite with partition coefficient [$D(Sr)^{Ms/gl}$] values ~0.5. Partitioning of Ba between biotite and melt appears to be temperature dependent, as shown in Figure 10A. Values of $D(Ba)^{Bt/gl}$

TABLE 5.—*Continued*

wt% oxides	7 + 5 700 R $n = 12$	7 + 4 750 F $n = 10$	8 + 6 700 F $n = 6$	8 + 7 750 F $n = 2$	5 + 15 650 R $n = 10$	5 + 14 650 R $n = 5$	7 + 10 650 R $n = 13$	8 + 6 700 F $n = 2$
	Biotite				**White mica**			
SiO_2	36.24(0.32)	35.64(0.19)	35.90(0.45)	34.85	47.45(0.51)	46.73(0.37)	45.16(0.39)	49.11
TiO_2	1.38(0.04)	1.71(0.03)	1.81(0.09)	1.83	0.40(0.04)	0.51(0.04)	0.58(0.02)	0.30
Al_2O_3	22.46(0.10)	22.35(0.27)	22.46(0.26)	20.86	29.96(0.22)	30.90(0.95)	32.64(0.40)	31.43
MgO	6.04(0.08)	7.24(0.07)	6.84(0.14)	7.44	1.72(0.04)	1.76(0.07)	1.66(0.06)	1.18
CaO	0.06(0.01)	0.02(0.01)	*0.02*	*0.02*	0.12(0.01)	0.10(0.03)	0.03(0.01)	0.05
MnO	0.37(0.01)	0.34(0.01)	0.33(0.02)	0.25	0.07(0.01)	0.07(0.01)	0.09(0.01)	0.09
FeO	14.09(0.14)	14.98(0.13)	15.71(0.29)	14.75	3.17(0.08)	3.31(0.07)	3.66(0.11)	2.03
NiO	0.35(0.08)	0.29(0.08)	0.41(0.10)	3.69	*0.04*	*0.04*	*0.04*	*0.04*
SrO	*0.07*	*0.07*	0.08(0.03)	*0.07*	0.22(0.04)	0.11(0.02)	*0.07*	0.11
BaO	2.39(0.12)	2.09(0.06)	2.66(0.18)	2.46	0.92(0.04)	1.18(0.07)	*0.13*	1.05
Na_2O	0.25(0.01)	0.22(0.01)	0.37(0.02)	0.40	0.69(0.02)	0.61(0.03)	0.44(0.02)	0.70
K_2O	7.94(0.03)	8.19(0.05)	7.88(0.11)	8.01	8.45(0.06)	7.95(0.35)	9.73(0.10)	8.42
Rb_2O	1.03(0.03)	1.12(0.03)	0.60(0.06)	0.50	1.03(0.02)	0.80(0.05)	0.86(0.02)	0.42
Cs_2O	0.37(0.05)	0.30(0.02)	0.20(0.08)	0.09	0.25(0.02)	0.25(0.03)	0.18(0.02)	0.10
H_2O	1.79	1.93(0.04)	2.54(0.02)	2.65	2.75	2.61(0.13)	2.79(0.04)	3.55
F	4.05(0.06)	3.86(0.09)	2.71(0.02)	2.39	31.5(0.09)	3.44(0.24)	3.12(0.06)	1.75
Li_2O								
Total	98.83	100.38	100.51	100.20	100.39	100.37	101.18	100.33
O = F	97.31	98.75	99.37	99.20	99.06	98.92	99.87	99.59
				Cations				
Si	5.62	5.47	5.46	5.39	6.51	6.41	6.16	6.58
$^{[4]}Al$	2.38	2.53	2.54	2.61	1.49	1.59	1.84	1.42
$^{[6]}Al$	1.73	1.51	1.50	1.19	3.35	3.40	3.42	3.54
Li								
Ti	0.16	0.20	0.21	0.21	0.04	0.05	0.06	0.03
Mg	1.40	1.66	1.55	1.71	0.35	0.36	0.34	0.24
Mn	0.04	0.03	0.04	0.03	0.01	0.01	0.01	0.01
Fe	1.83	1.92	2.00	1.91	0.36	0.38	0.42	0.23
Ni	0.04	0.04	0.05	0.46	0.00	0.00	0.00	0.00
Ca	0.01	0.00	0.00	0.00	0.02	0.01	0.00	0.01
Sr	0.00	0.00	0.01	0.00	0.00	0.00	0.00	0.01
Ba	0.15	0.13	0.16	0.15	0.05	0.06	0.00	0.06
Na	0.08	0.07	0.11	0.12	0.18	0.16	0.12	0.18
K	1.57	1.60	1.53	1.58	1.48	1.39	1.69	1.44
Rb	0.10	0.11	0.06	0.05	0.09	0.07	0.08	0.04
Cs	0.02	0.02	0.01	0.01	0.01	0.01	0.01	0.01
OH	1.85	1.98	2.58	2.73	2.52	2.39	2.54	3.17
F	1.99	1.87	1.30	1.17	1.37	1.49	1.35	0.74
Total	15.13	15.29	15.23	15.42	13.94	13.90	14.15	13.80
Mg′	0.43	0.46	0.43	0.47	0.49	0.48	0.44	0.50

decrease from ~16 to 3 over the temperature range of 650–750 °C. The Mg′ varies only slightly in biotite from these experiments; therefore, we can unequivocally say that the large range of $D(Ba)^{Bt/gl}$ recognized here does not correlate with changes in Mg′ (cf. Guo and Green, 1990). White mica also preferentially harbors Ba over melt with a range of values between ~3.5 and 5.5, but Table 8 demonstrates that Ba is preferentially partitioned into biotite over white mica.

TABLE 6. SIMS probe analyses of biotite and white mica

Experiment	4-6	5-11	SM-7	7 + 10
		Biotite		
Li	813	3525	164	5890
Rb	870	10375	2600	10662
Sr	5	6	5	5
Cs	29	4745	65	8166
Ba	1170	704	65	555
		White mica		
Li	830			
Rb	753			
Sr	6			
Cs	25			
Ba	828			

Note: Values are parts per million by weight.

Na, K, Rb, and Cs

The partition coefficient for Rb between biotite and glass is ~2 and remains essentially constant over the temperature interval investigated (Fig. 10B). Rb also partitions into white mica over glass with values ≤ 2; thus, Rb partitioning between coexisting biotite-white mica pairs is slightly greater than unity at 650 °C (Table 8). Cs is the only element studied in this system that is preferentially partitioned into melt over any mineral (including alkali feldspars). Values of $D(Cs)^{Bt/gl}$ vary from 0.27 to 0.49 (±0.03), whereas values of $D(Cs)^{Ms/gl}$ range from 0.16 to 0.24 (±0.02), so that partitioning of Cs between coexisting biotite and muscovite is also near unity at 650 °C. Cs partitioning into biotite does not appear to be temperature dependent (Fig. 11A), at least over the temperature interval investigated. Results obtained by SIMS analyses are generally in agreement with the values re-

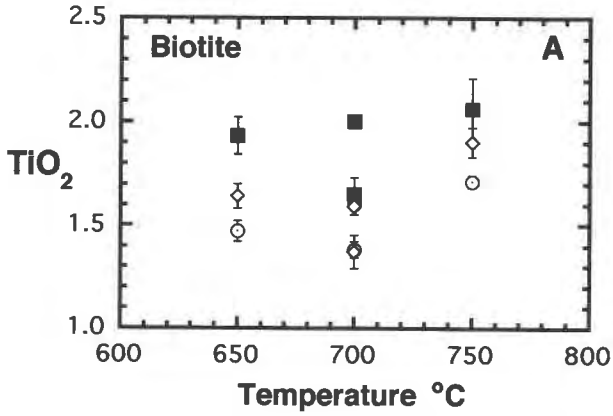

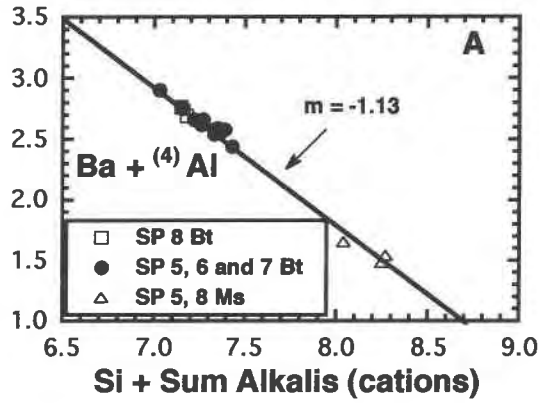

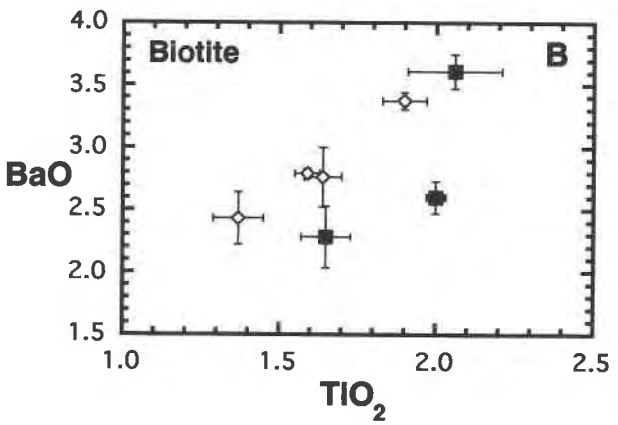

Fig. 8. (**A**) TiO_2 vs. temperature for Synpel biotites. (**B**) TiO_2 vs. BaO for Synpel biotites. Symbols as in Fig. 3A.

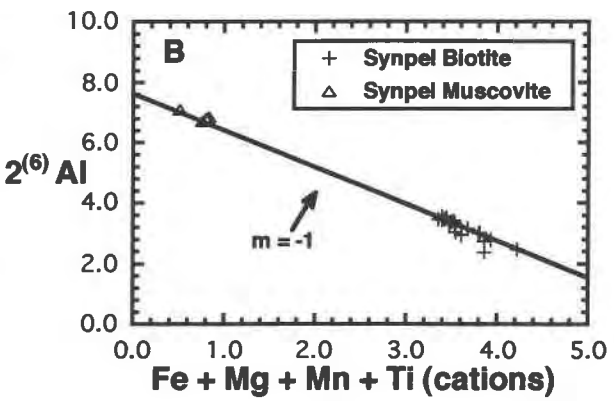

Fig. 9. (**A**) Proposed substitution mechanism for Ba into Synpel biotite and white mica (muscovite): $^{[12]}Ba^{2+} + {}^{[4]}Al^{3+} = {}^{[4]}Si^{4+} + {}^{[12]}(K + Na + Cs + Rb)^{1+}$ (in cations). (**B**) Proposed substitution mechanism for Ti in octahedral sites into Synpel biotite and white mica: $^{[6]}Ti^{4+} + {}^{[6]}(Mg + Mn + Fe)^{2+} = 2^{[6]}Al^{3+}$ (in cations).

ported above. Values of $D(Rb)^{Bt/gl}$ in experiments SP5-11, SP7+10, and SM-7 vary from 1.51 to 1.76; $D(Cs)^{Bt/gl}$ values range between 0.51 and 0.70. Partition coefficients for experiment SP4-6, which lacked the Rb- and Cs-rich biotite, are slightly lower for both Rb [$D(Rb)^{Bt/gl} = 1.11$; $D(Rb)^{Ms/gl} = 0.96$] and Cs [$D(Cs)^{Bt/gl} = 0.41$; $D(Cs)^{Ms/gl} = 0.36$]. Note, however, that these values are similar to or overlap with partition coefficient values obtained by EMPA (Table 7).

TABLE 7. Partition coefficients among biotite, muscovite, and melt

	6 + 6 $D^{Bt/gl}$	6 + 7 $D^{Bt/gl}$	6 + 5 $D^{Bt/gl}$	6 + 4 $D^{Bt/gl}$	7 + 10 $D^{Bt/gl}$	7 + 6 $D^{Bt/gl}$
Si	0.56(0.00)	0.60(0.01)	0.55(0.01)	0.55(0.00)	0.58(0.01)	0.56(0.01)
Ti	>48.25	27.50(1.92)	40.00(5.15)	22.89(2.07)	21.86(3.63)	24.50(3.29)
Al	1.40(0.01)	1.31(0.01)	1.28(0.01)	1.15(0.01)	1.43(0.02)	1.39(0.01)
Mg	133.00(13.48)	85.71(2.47)	84.29(5.62)	67.33(2.71)	73.63(18.56)	76.25(12.39)
Ca	0.05(0.02)	0.08(0.02)	<0.03	0.03(0.01)	0.02(0.01)	0.03(0.01)
Mn	7.60(0.50)	4.50(0.28)	5.50(0.51)	3.71(0.19)	6.83(0.63)	5.57(0.27)
Fe	32.28(1.07)	22.19(0.30)	27.96(0.58)	18.42(0.32)	28.45(3.03)	27.89(1.69)
Ni	>11.25	>14.25	>64.29	>4.57		>2.29
Sr	0.64(0.19)	<0.37	0.22(0.07)	<0.14		<0.36
Ba	28.66(3.07)	9.12(1.08)	11.30(1.01)	8.02(0.39)	<1.19	14.33(2.85)
Na	0.17(0.00)	0.21(0.01)	0.16(0.00)	0.16(0.01)	0.13(0.01)	0.11(0.01)
K	2.26(0.02)	2.19(0.03)	2.16(0.01)	1.98(0.02)	2.24(0.05)	2.32(0.04)
Rb	1.90(0.08)	2.05(0.11)	1.97(0.02)	1.83(0.06)	2.04(0.15)	1.76(0.11)
Cs	0.28(0.03)	0.35(0.06)	0.38(0.04)	0.36(0.03)	0.31(0.06)	0.31(0.05)
F	1.98(0.05)	1.75(0.11)	1.60(0.04)	1.82(0.04)	2.28(0.11)	2.11(0.05)
Li					1.64	

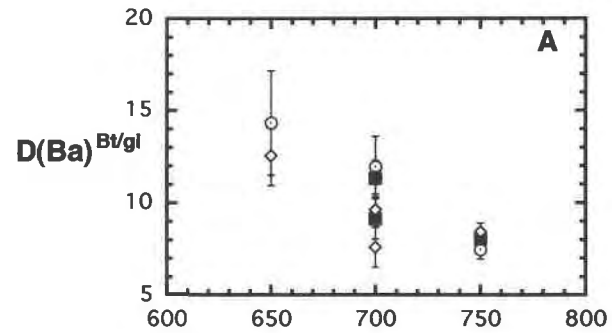

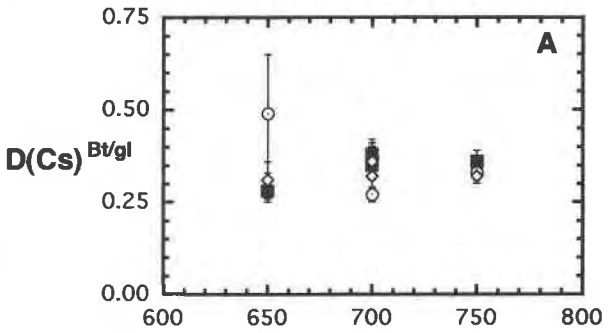

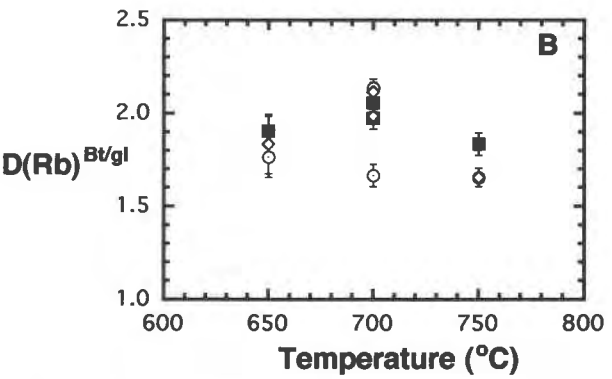

Fig. 10. Temperature dependence of distribution coefficients: (**A**) $D(Ba)^{Bt/gl}$ shows a strong decrease with increasing temperature. (**B**) $D(Rb)^{Bt/gl}$ shows no correlation with temperature. Error bars represent 1σ errors. Symbols as in Fig. 3A.

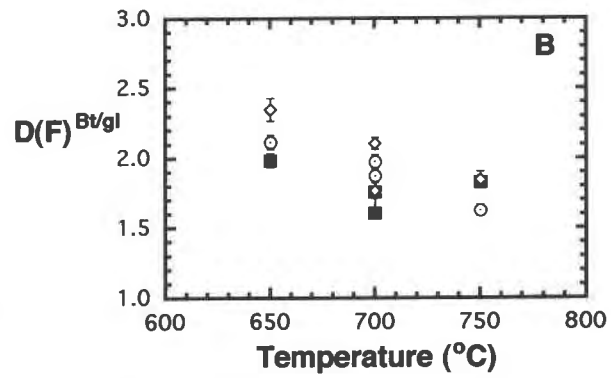

Fig. 11. Temperature dependence of distribution coefficients: (**A**) $D(Cs)^{Bt/gl}$ shows no correlation with temperature. (**B**) $D(F)^{Bt/gl}$ shows a decrease with increasing temperature. Error bars represent 1σ errors. Symbols as in Fig. 3A.

F

The partition coefficients for F between biotite and glass (ranging from ~1.8 to 2.5) are unexpectedly low, as discussed below. Low values were also determined in other Li-poor metaluminous to peraluminous experiments and in several natural analogs (Patiño Douce and Johnston, 1991; Skjerlie and Johnston, 1992; Icenhower and London, 1993); thus, Li is not uniquely responsible for this partitioning behavior. Distributions of F between biotite and melt also have a slight negative correlation with temperature, as illustrated in Figure 11B. Although we expect that a range of Mg′ values in biotite should affect $D(F)^{Bt/gl}$,

TABLE 7.—*Continued*

	7 + 7 $D^{Bt/gl}$	7 + 5 $D^{Bt/gl}$	7 + 4 $D^{Bt/gl}$	5 + 14 $D^{Bt/gl}$	5 + 15 $D^{Bt/gl}$	5 + 8 $D^{Bt/gl}$
Si	0.58(0.00)	0.58(0.01)	0.59(0.00)	0.58(0.01)	0.57(0.00)	0.56(0.01)
Ti	26.67(3.94)	19.71(2.25)	19.00(1.47)	22.29(3.21)	19.11(2.05)	27.33(4.82)
Al	1.33(0.01)	1.31(0.01)	1.21(0.01)	1.43(0.01)	1.42(0.01)	1.38(0.02)
Mg	74.00(5.37)	54.91(6.49)	72.40(8.13)	54.55(9.94)	37.63(4.75)	50.42(8.77)
Ca	<0.02	0.05(0.01)	0.02(0.22)	0.05(0.01)	0.05(0.00)	0.06(0.02)
Mn	3.75(0.42)	4.63(0.32)	3.78(0.87)	4.86(0.17)	5.43(0.38)	4.25(0.31)
Fe	20.75(0.56)	21.03(0.99)	17.83	23.38(1.47)	20.19(1.65)	23.69(2.13)
Ni		>10.00	>8.29	>1.00		>8.57
Sr	<0.18	<0.03	<0.11	0.38(0.21)	<0.16	<0.32
Ba	11.95(1.66)	11.38(0.92)	7.46(0.52)	15.67(3.04)	12.67(1.52)	12.55(1.62)
Na	0.13(0.00)	0.12(0.01)	0.13(0.01)	0.23(0.01)	0.18(0.01)	0.16(0.02)
K	2.10(0.01)	1.89(0.01)	1.67(0.02)	2.36(0.04)	2.26(0.03)	2.26(0.05)
Rb	2.13(0.05)	1.66(0.06)	1.65(0.05)	1.84(0.10)	1.75(0.07)	1.83(0.16)
Cs	0.32(0.04)	0.36(0.05)	0.32(0.02)	0.28(0.04)	0.28(0.03)	0.49(0.16)
F	1.97(0.05)	1.87(0.05)	1.62(0.04)	2.34(0.10)	2.33(0.06)	2.34(0.08)
Li						

the small range of values of Mg′ in these experiments precluded a test of this assumption (although see Icenhower and London, 1993). F partitions in favor of white mica over melt with values ~1.8. Thus, at 650 °C, $D(F)^{Bt/Ms}$ is near unity (Table 8).

Discussion

Melting reactions and the stability of muscovite

The upper stability limit of muscovite in granitic magmas has been the topic of numerous investigations, including Yoder and Eugster (1955), Storre (1972), Storre and Karotke (1971, 1972), Chatterjee and Johannes (1974), Chatterjee and Flux (1986), Miller et al. (1981), Anderson and Rowley (1981), and Zen (1988). The reaction of the second sillimanite isograd, muscovite + quartz = orthoclase + aluminum silicate + H_2O, crosses the H_2O-saturated haplogranite solidus, elucidated by Tuttle and Bowen (1958) and Merrill et al. (1970), at ~300 MPa and 660 °C (cf. Althaus et al., 1970). The stable portion of the melting reaction that we observed, albite + quartz + muscovite + H_2O = melt + aluminum silicate, lies on the high-pressure side of the invariant point formed by the two reactions above (e.g., Storre and Karotke, 1971); hence, melting in our experiments occurred along the metastable extension of this reaction to 200 MPa. The solidus of the Synpel systems at 625 °C (with and without biotite) lies close to but below the metastable extension of the reaction albite + quartz + muscovite + H_2O = melt + aluminum silicate, as reported by Storre and Karotke (1971). Similar bulk compositions, with starting muscovite from Spruce Pine, North Carolina, that is lower in Li and F than STK-127, melt between 650 and 700 °C at 200 MPa (Michael B. Wolf, unpublished data, 1994). We attribute the lower apparent solidus of our Synpel system to the presence of F that creates an identifiable fraction of melt at lower temperatures. As noted previously, the bulk compositions of Synpel were chosen so as to eliminate quartz at the eutectic; hence, both aluminum silicate and Fe-Ti–enriched corundum are present just above the solidus in these experiments.

Table 8. Partitioning of elements among biotite, muscovite, and melt

	Synpel				Others		
	650 °C*			700 °C**	1	2	3
	Bt/gl	Ms/gl	Bt/Ms	Bt/Ms	Bt/Ms	Bt/Ms	Bt/Ms
Ti	22.0	6.7	3.3	5.9	12.0		5.6
Mg	55.4	15.8	3.5	5.8	52.5		9.5
Fe	24.5	5.5	4.5	7.8	19.7		17.0
Mn	6.0	1.2	5.0	3.6	2.8		
Ba	14.4	4.5	3.2	2.5	2.9		1.1
Rb	1.9	1.6	1.2	1.5	1.1	2.5	1.5
Cs	0.3	0.2	1.3	2.1		6.0	2.7
F	2.3	1.8	1.3	1.6		2.0	1.7
Li	1.7	0.8	2.1			2.0	3.5

Note: 1 = Pichavant et al., 1988; 2 = Shearer et al., 1986; 3 = Neiva et al., 1987.
* Data for 650 °C are from experiments SP5, SP6, and SP7.
** Data for 700 °C are from experiment SP8.

In the quartz-absent system the next reaction encountered is the one terminal to muscovite: muscovite = orthoclase + corundum + H_2O. Unlike the melting reaction above, this is a stable reaction at the pressure and temperatures of our experiments. Our results are similar to (though better bracketed than) those reported by Yoder and Eugster (1955) and about 30–50 °C higher than the results of Evans (1965), Velde (1966), and Huang et al. (1973). The persistence of Ms to higher temperature in our system might be attributed to solid solutions (toward biotite) involving Fe and Ti that have been proposed to extend the stability of white mica to higher temperatures (e.g., Anderson and Rowley, 1981; Centanni, 1983, 1985; see Zen, 1988). Substitution toward paragonite, however, apparently decreases the thermal stability of muscovite (e.g., Chatterjee and Flux, 1986). From Table 3, the white micas grown in our reversed experiments have compositions very close to those of natural igneous white micas (Miller et al., 1981; Ferrow et al., 1990), and hence the reaction boundary at about 715 °C and 200 MPa (H_2O)

Table 7.—*Continued*

	5 + 9 $D^{Bt/gl}$	5 + 7 $D^{Bt/gl}$	5 + 6 $D^{Bt/gl}$	4-6 $D^{Bt/gl}$	5-11 $D^{Bt/gl}$	SM-7 $D^{Bt/gl}$	4-6 $D^{Ms/gl}$	5 + 14 $D^{Ms/gl}$	5 + 15 $D^{Ms/gl}$	7 + 10 $D^{Ms/gl}$	Macusani $D^{Bt/gl}$
Si	0.57(0.00)	0.57(0.00)	0.58(0.00)					0.73(0.01)	0.74(0.01)	0.69(0.01)	
Ti	17.67(3.75)	19.57(4.80)	23.75(3.09)					7.29(1.19)	4.44(0.59)	8.29(1.36)	80.75
Al	1.36(0.01)	1.27(0.01)	1.24(0.01)					1.97(0.06)	1.89(0.02)	2.06(0.03)	
Mg	68.78(12.10)	49.54(14.80)	76.00(0.66)					16.00(2.98)	10.75(1.38)	20.75(5.27)	210
Ca	0.02(0.01)	>0.02	0.03(0.01)					0.12(0.04)	0.14(0.02)	0.03(0.01)	
Mn	3.25(0.28)	5.00(0.48)	3.50(0.45)					1.00(0.14)	1.00(0.12)	1.50(0.15)	2.67
Fe	20.49(1.36)	19.60(2.69)	16.80(0.22)					5.17(0.34)	4.28(0.37)	6.91(0.76)	39.91
Ni	>13.43	>58.00	>10.50								
Sr	<0.17	<0.17	<0.23	0.04	0.03	0.06	0.06	0.52(0.12)	0.49(0.09)		
Ba	9.62(0.65)	7.59(1.08)	8.43(0.46)	11.50	5.63	12.26	8.14	5.62(1.12)	3.41(0.42)		
Na	0.17(0.01)	0.15(0.01)	0.15(0.01)					0.40(0.03)	0.35(0.01)	0.24(0.01)	
K	2.23(0.03)	2.05(0.03)	1.80(0.01)					2.54(0.12)	2.58(0.04)	2.46(0.05)	
Rb	2.11(0.07)	1.98(0.07)	1.65(0.05)	1.11	1.51	1.73	0.96	1.51(0.11)	1.75(0.04)	1.56(0.05)	1.54
Cs	0.27(0.02)	0.37(0.03)	0.33(0.02)	0.41	0.51	0.57	0.36	0.23(0.03)	0.24(0.02)	0.16(0.02)	
F	2.10(0.04)	1.76(0.14)	1.84(0.06)					1.92(0.15)	1.81(0.07)	1.68(0.08)	1.57
Li				0.80	1.01	1.67	0.82				

represents a practical, if not end-member, stability limit for white mica.

Melt compositions

Melt compositions in the Synpel 4 system (biotite absent) are notably peraluminous with ASI values of muscovite-saturated near-minimum melts (650 °C) ranging from 1.3 to 1.4 (Table 3). At higher temperatures, these same ASI values pertain to corundum-saturated melts. In an unrelated study, London et al. (1993) similarly found that melts in the hydrous peraluminous haplogranite system were buffered by corundum saturation at the ASI value of 1.35. These results show more congruency in the melting of muscovite and a more strongly peraluminous composition than previously assumed for melting a typical metapelite (e.g., White and Chappell, 1983). The very peraluminous compositions could be augmented by the presence of F in these low-temperature melts (glasses contain about 2 wt% normative cryolite component). The percentage of melting to be anticipated from a particular rock type is, of course, determined also by how far the bulk composition of the rock lies from the minimum melt composition (cf. Vielzeuf and Holloway, 1988; Patiño Douce and Johnston, 1991).

Low concentrations of femic components in H_2O-undersaturated experimental peraluminous melts have been used by other investigators to argue for the presence of entrained restite in natural whole-rock samples that contain relatively high concentrations (>3 wt%) of femic components (e.g., Patiño Douce and Johnston, 1991). Our H_2O-saturated experiments yield the same low total solubilities for femic components as the H_2O-undersaturated results.

Biotite reactions

The composition of biotite grown from melt changes with temperature from the minimum (involving melting of albite-quartz-muscovite) to 750 °C. This behavior indicates that biotite reacts continuously with melt over the temperature interval of the experiments and does not represent an inert component, reacting only by way of melting, as implied by Vielzeuf and Holloway (1988) and others. These results have an important bearing on the trace-element signatures of low-temperature S-type melts, which, though they may derive negligible biotite (components) by melting, may nevertheless achieve an equilibrium (by recrystallization of biotite) with regard to major- and trace-element distributions between biotite and that melt.

Our results demonstrate that biotite becomes more magnesian and serves as source of Fe, Mn, Rb, Cs, and F to the melt. Patiño Douce and Johnston (1991) also noted that biotite compositions change systematically with temperature but found that F concentrations increased strongly in residual biotite.

Element partitioning

Results obtained by SIMS analyses provide useful comparisons to results obtained by EMPA. Partition coefficients for Rb, Cs, Sr, and Ba in SM-7 (Spor Mountain rhyolite) between biotite and melt are nearly identical to those obtained on Synpel compositions, despite the significant differences in LILE concentrations and the ASI values of these melts (Table 7). One conclusion is that Rb, Cs, Sr, and Ba behave as dilute components up to several weight percent in both biotite and melt, and hence the partitioning values determined for Synpel have relevance to the normally trace levels of LILEs in natural systems. The partitioning of these LILEs between biotite and melt also appears to be independent of Li content (98 ppmw in Spor Mountain, >3000 ppmw in Synpel), and of ASI (SM-7 has an ASI of 1.1). At least for this suite of trace elements, therefore, partition coefficients determined from metaluminous silicic systems may also be pertinent to peraluminous compositions.

Partitioning of rare alkalis. We have yet to resolve fully the behavior of Li in peraluminous melts. The existing data suggest, however, that $D(\mathrm{Li})^{Bt/gl}$ is temperature dependent; values vary from ~1.65 at 650 °C (SP7+10) to ~1 at 750 °C (SP5-11). We tentatively conclude that the partition coefficient for Li between white mica and melt is similar to that for biotite, at a value near unity. Although biotite harbors a large fraction of Li to temperatures (when the bulk of biotite melts) well above the minimum, the Li content of muscovite is contributed when melting commences around 650 °C and when muscovite alone breaks down to orthoclase + corundum. Therefore, melting or even reequilibration of biotite with melt is not required as a source for Li. White mica alone can contribute a large quantity of Li at low temperatures. The contribution from muscovite is especially significant for typical metapelites that contain a very large modal fraction of muscovite. These rocks generate only a small fraction of low-temperature melt (they lack the necessary albite component), but the breakdown of muscovite to orthoclase component of alkali feldspar plus aluminum silicate or corundum at ≥715 °C could contribute large quantities of Li into a small fraction of melt. In this way, Li-rich granitic pegmatites could be generated by a small fraction of melting from initially mica-rich protoliths (e.g., Stewart, 1978).

Rb partitions in favor of both biotite and white mica over melt with values within the range reported in the literature (see Jolliff et al., 1992, for a review). Partitioning of Cs between white mica and melt is also within the range of values reported in the literature, but our results for biotite disagree with previous studies. Other investigators have consistently determined partition coefficients for Cs in biotite greater than unity (cf. Mahood and Hildreth, 1983; Walker et al., 1989; Nash and Crecraft, 1985), whereas we obtained values substantially below one. Although the determination of partition coefficients by separation of phenocrysts and coexisting glass has been criticized by several workers, including Michael (1988) and Sisson (1991), we cannot imagine an accessory phase included in normal igneous biotite that is significantly richer in Cs than the biotite itself. Our results are reproducible and are not subject to the uncertainties associated with

phenocryst-glass groundmass separation and analysis. Moreover, we can state unequivocally that the biotite produced in these experiments crystallized from melt, and hence that the partition coefficient for Cs is valid. We speculate only that the partitioning of Cs may be different under different conditions of crystallization, with different biotite compositions, or that the previously determined values do not represent equilibrium mineral-melt pairs (i.e., the biotite is residual, xenocrystic, or hydrothermally recrystallized).

The continuous reaction of biotite with melt fractionates Rb from Cs, with Rb retained to higher temperatures in biotite. As in the case of Li, extensive melting of muscovite at the inception of anatexis does not fractionate Rb from Cs; the Rb-Cs signature of melt is the same as that of the original white mica. White mica that persists through initial melting breaks down to orthoclase + aluminum silicate or corundum at only slightly higher temperatures. Rb is far more compatible in biotite and alkali feldspar (Icenhower and London, in preparation) than is Cs, so that the terminal reaction of muscovite liberates Cs to melt, with a large fraction of Rb retained in newly formed alkali feldspar. In this way, peraluminous melts may acquire the LCT (Li-Cs-Ta) signature recognized by Cerny (1992).

Partitioning of Ba. Partitioning of Ba between biotite and melt appears to be strongly influenced by temperature, as discussed above (see Fig. 10A). Our biotite data suggest that although concentrations of TiO_2 and BaO appear to correlate, there is no evidence that Ti concentrations affect Ba partitioning in any significant way, as discussed above.

Our data demonstrate that Ba is partitioned preferentially into biotite compared with coexisting white mica (Table 8). Our SIMS probe data from undoped (with respect to Ba) experiments indicate generally high $D(\mathrm{Ba})^{\mathrm{Bt/gl}}$ values (~6–13) compared with reported muscovite-melt partition coefficients. Data determined on natural igneous systems appear to support Ba distribution in favor of biotite. For example, Ba partitions in favor of biotite over white mica in three out of four applicable samples from the Serra da Estrela granite, Portugal (Neiva et al., 1987). A single coexisting biotite-white mica pair from the Macusani volcanics, Peru, indicates that Ba partitions in favor of biotite [$C(\mathrm{Ba})^{\mathrm{Bt}}/C(\mathrm{Ba})^{\mathrm{Ms}} = 2.9$, where C is concentration in parts per million by weight] (Pichavant et al., 1988). Finally, Ba concentrations determined on coexisting biotite-white mica pairs in the altered Abas granite, Portugal, indicate that Ba is preferentially incorporated by biotite (Konings et al., 1988).

Other investigations do not, however, confirm the above results. Ba partitions in favor of white mica (=muscovite) over biotite in metamorphic assemblages (e.g., Dahl et al., 1993; Harlow, 1991; Hervig and Peacock, 1989; Shearer et al., 1986) and predominately, although not exclusively, in granitic systems (Lee et al., 1981; Neiva and Gomes, 1991; Silva and Neiva, 1990; Kretz et al., 1989; de Albuquerque, 1975; Bea et al., 1994).

It is not known whether crystal-chemical controls on Ba partitioning or the mobility of Ba during postcrystallization processes can explain this range of data. Haack et al. (1984) suggested that Ba is strongly mobilized from metapelites during episodes of regional metamorphism whereas Rb is not. This may explain the observation that Ba values in muscovite are highly variable with respect to other elements, such as Rb (Jolliff et al., 1992; cf. their Fig. 5). Although the partition coefficients from this study agree well with values measured from the Macusani volcanics, partition coefficients for Ba between white and dark micas are not yet meaningful or reliable for metamorphic or plutonic igneous rocks.

Partitioning of F. Silicic rocks rich in F have been reported by numerous investigators (e.g., Burt et al., 1982; Christiansen et al., 1980, 1984). The prevailing model for the generation of these rocks is the remelting of a dehydrated protolith containing F-enriched biotite. This model is based on the recognition of F-rich biotite in high-grade metamorphic terranes (e.g., Guidotti, 1984), the observation that F extends the stability of biotite to higher temperatures (Munoz, 1984; Peterson et al., 1991), and the presumption that F is strongly partitioned into biotite during episodes of partial melting. A surprising result of our study is that F partitions into biotite and white mica over melt but not as strongly as expected. This result is consistent with the work of Patiño Douce and Johnston (1991) and Skjerlie and Johnston (1992) on peraluminous melts generated by experimental partial fusion of natural biotite- and amphibole-bearing tonalitic gneisses. Although the values of $D(\mathrm{F})^{\mathrm{Bt/gl}}$ that they reported (4–10) are higher than ours, this can be accounted for by the significantly higher temperatures (>800 °C) of their experiments. The higher temperatures of their experiments probably also explain their observation that concentrations of F in biotite increase with temperature, especially above 925 °C. We thus conclude that values of $D(\mathrm{F})^{\mathrm{Bt/gl}}$ at the inception of hydrous partial melting are small (~2 biotite, ~1.8 white mica).

Despite the high Li content of the Synpel melt and recrystallized biotite, the values of $D(\mathrm{F})^{\mathrm{Bt/gl}}$ are lower at the same Mg′ than those of biotite-glass pairs from the Li-poor Spor Mountain rhyolite (Icenhower and London, 1993). Tentatively, the best explanation for low partition coefficients, even for this Li-rich composition, is that the Synpel melts are strongly peraluminous, and that excess Al substantially and selectively increases the solubility of F in melt. In any case, the quantity of F liberated to low-temperature anatectic melts is determined by bulk melting of white mica and recrystallization (or the lack of it) in biotite. If biotite (and white mica that survives melting) recrystallizes in the presence of melt, then the small partition coefficients explain how S-type magmas with the chemical signatures of low-temperature melts (e.g., elevated B, Be, and Cs, as in Hercynian granites of western Europe) can acquire their high F content. The hypothesis that F-rich granitic melts originate only at high temperatures from rocks that have previously undergone anatexis is not unique.

Comparison of the experimental results with natural systems

Finding a reliable analog to the melt compositions generated here is difficult. Most comparable rocks are plutonic (pegmatites or granites) and have undergone extensive hydrothermal reequilibration. Partially vitric rhyolite from the Macusani volcanic province, Peru, provides the best possible comparison with the Li- and F-rich and peraluminous compositions generated by melting of Synpel (London et al., 1988, 1989; Pichavant et al., 1987, 1988). That comparison, detailed in Table 7, shows what we consider to be a remarkable consistency between experimental and natural mineral-glass partition coefficients. Note that the partitioning of Rb and F (among others) follows the trends established in this experimental study, not those previously determined on mineral separates or by other methods that are potentially problematic. We reiterate, however, that the results obtained from the study of Synpel appear to be applicable to melt compositions that are metaluminous and much lower in Li (i.e., Spor Mountain), and hence that the results extend to a wider range of igneous rocks than just the Macusani volcanics.

Trace-element equilibration between restite and melt

A potentially important extension of this experimental work pertains to our observation that once melt forms, residual biotite and muscovite (the abundances of which in the system are greater than the concentrations needed for saturation of melt) recrystallize to attain a continuous equilibrium with melt as temperature changes. The effect on melt composition is that its trace-element signature is derived from reaction with the entire volume of residual mica (biotite only above 700 °C), not just the small fraction of mica that actually melts.

Additionally, one might test this observation by comparison of empirical partition coefficients between micas and glass (or reconstituted glass from matrix analysis). Disparities in apparent partition coefficients could reflect a lack of reequilibration and, hence, an absence of recrystallization of the residual phase. Conversely, if residual phases attain an equilibrium partitioning of trace elements with melt, then this equilibration makes it more difficult to recognize residual phases in igneous rocks.

Acknowledgments

This work represents a portion of a Ph.D. dissertation by J.I. Financial support for this research was provided by NSF-EPSCoR contract EHR-9108771 to D.L. for collaborative research with the University of Tulsa. The Electron Microprobe Laboratory was created by grant DE-FG22-87FE1146 to D.L. from the U.S. Department of Energy, and experimental facilities were established and maintained by grants EAR-8516753, EAR-8720498, and EAR-8821950 to D.L. from the National Science Foundation. J.I. thanks the GSA Penrose Foundation for support of ion microprobe analysis. We thank George Morgan and Graham Layne for aid in electron microprobe and secondary-ion mass spectrometry analyses. We thank Dana Johnston, Brad Jolliff, Ed Hansen, George Morgan, Mike Wolf, and Rebecca Ambers for insightful and constructive reviews.

References cited

Althaus, E., Karotke, E., Nitsch, K.H., and Winkler, H.G.F. (1970) An experimental re-examination of the upper stability limit of muscovite plus quartz. Neues Jahrbuch für Mineralogie Monatshefte, 325–336.

Anderson, J.L., and Rowley, M.C. (1981) Synkinematic intrusion of peraluminous and associated metaluminous granitic magmas, Whipple Mountains, California. Canadian Mineralogist, 19, 83–101.

Arth, J.G. (1976) Behavior of trace elements during magmatic processes: A summary of the theoretical models and their applications. U.S. Geological Survey Journal of Research, 4, 41–47.

Bea, F., Pereira, M.D., and Stroh, A. (1994) Mineral/leucosome trace-element partitioning in a peraluminous migmatite (a laser ablation-ICP-MS study). Chemical Geology, 117, 291–312.

Beattie, P., Drake, M., Jones, J., Leeman, W., Longhi, J., McKay, G., Nielsen, R., Palme, H., Shaw, D., Takahashi, E., and Watson, B. (1993) Teminology for trace-element partitioning. Geochimica et Cosmochimica Acta, 57, 1605–1606.

Brigatti, M.F., and Poppi, L. (1993) Crystal chemistry of Ba-rich trioctahedral micas-1*M*. European Journal of Mineralogy, 5, 857–871.

Burt, D.M., Bikun, J.V., and Christiansen, E.H. (1982) Topaz rhyolites: Distribution, origin, and significance for exploration. Economic Geology, 77, 1818–1836.

Centanni, J.P. (1983) The composition, synthesis and thermal stability of celadonitic muscovite with regards to its occurrence in plutonic rocks, 67 p. Master's thesis, University of California, Santa Barbara, California.

——— (1985) Composition, synthesis and thermal stability of celadonitic white mica: Implications for plutonic muscovite. Geological Society of America Abstracts with Programs, 17, 347.

Cerny, P. (1992) Fertile granites of Precambrian rare-element pegmatite fields: Is geochemistry controlled by tectonic setting or source lithologies? Precambrian Research, 51, 429–468.

Chatterjee, N.D., and Flux, S. (1986) Thermodynamic mixing properties of muscovite-paragonite crystalline solutions at high temperatures and pressures, and their geological applications. Journal of Petrology, 27, 677–693.

Chatterjee, N.D., and Johannes, W. (1974) Thermal stability and standard thermodynamic properties of synthetic $2M_1$-muscovite, $KAl_2[AlSi_3O_{10}(OH)_2]$. Contributions to Mineralogy and Petrology, 48, 89–114.

Christiansen, E.H., Bikun, J.V., and Burt, D.M. (1980) Petrology and geochemistry of topaz rhyolites, western United States. U.S. Department of Energy Open-File Report GJBX-225, 80, 37–122.

Christiansen, E.H., Bikun, J.V., Sheridan, M.F., and Burt, D.M. (1984) Geochemical evolution of topaz rhyolites from the Thomas Range and Spor Mountain, Utah. American Mineralogist, 69, 223–236.

Dahl, P.S., Wehn, D.C., and Feldman, S.G. (1993) The systematics of trace-element partitioning between coexisting muscovite and biotite in metamorphic rocks from the Black Hills, South Dakota, USA. Geochimica et Cosmochimica Acta, 57, 2487–2505.

de Albuquerque, C.A.R. (1975) Partition of trace elements in co-existing biotite, muscovite and potassium feldspar of granitic rocks, Northern Portugal. Chemical Geology, 16, 89–108.

Dymek, R.F. (1983) Titanium, aluminum and interlayer cation substitutions in biotite from high-grade gneisses, West Greenland. American Mineralogist, 68, 880–899.

Evans, B.W. (1965) Application of a reaction rate method to the breakdown equilibria of muscovite and muscovite plus quartz. American Journal of Science, 263, 647–667.

Ferrow, E.A., London, D., Goodman, K.S., and Veblen, D.R. (1990) Sheet silicates of the Lawler Peak granite, Arizona: Chemistry, structural variations, and exsolution. Contributions to Mineralogy and Petrology, 105, 491–501.

Guidotti, C.V. (1984) Micas in metamorphic rocks. In Mineralogical Society of America Reviews of Mineralogy, 13, 357–467.

Guo, J., and Green, T.H. (1990) Experimental study of barium partitioning between phlogopite and silicate liquid at upper-mantle pressure and temperature. Lithos, 24, 83–95.

Haack, U., Heinrichs, H., Boneß, M., and Schneider, A. (1984) Loss of

metals from pelites during regional metamorphism. Contributions to Mineralogy and Petrology, 85, 116–132.

Hall, A., Jarvis, K.E., and Walsh, J.N. (1993) The variation of cesium and 37 other elements in the Sardinian granite batholith, and the significance of cesium for granite petrogenesis. Contributions to Mineralogy and Petrology, 114, 160–170.

Hanson, G.N. (1978) The application of trace elements to the petrogenesis of rocks of granitic composition. Earth and Planetary Science Letters, 38, 26–43.

Harlow, G.E. (1991) Barium enriched true micas from metasomatized inclusions in serpentinite, Motagua Valley, Guatemala. Geological Society of America Abstracts with Programs, 23(5), A219.

Harris, N.B.W., and Inger, S. (1992) Trace element modelling of pelite-derived granites. Contributions to Mineralogy and Petrology, 110, 46–56.

Hervig, R.L., and Peacock, S.M. (1989) Water and trace elements in coexisting muscovite and biotite from metamorphic rocks. Eos, 70(15), 490.

Higuchi, H., and Nagasawa, H. (1969) Partition of trace elements between rock-forming minerals and the host volcanic rocks. Earth and Planetary Science Letters, 7, 281–287.

Hogan, J.P., and Sinha, A.K. (1991) The effect of accessory minerals on the redistribution of lead isotopes during crustal anatexis: A model. Geochimica et Cosmochimica Acta, 55, 335–348.

Huang, W.L., Robertson, J.K., and Wiley, P.J. (1973) Melting relations of muscovite to 30 kilobars in the system $KAlSi_3O_8$-Al_2O_3-H_2O. American Journal of Science, 273, 415–427.

Icenhower, J.P., and London, D. (1993) An experimental study of the partitioning of fluorine between biotite and silicic melts. Geological Society of America Abstracts with Programs, 25(6), A-372.

Jolliff, B.L., Papike, J.J., and Shearer, C.K. (1992) Petrogenetic relationships between pegmatite and granite based on geochemistry of muscovite in pegmatite wall zones, Black Hills, South Dakota, USA. Geochimica et Cosmochimica Acta, 56, 1915–1939.

Konings, R.J.M., Boland, J.N., Vriend, S.P., and Jansen, J.B.H. (1988) Chemistry of biotites and muscovites in the Abas granite, northern Portugal. American Mineralogist, 73, 754–765.

Kretz, R., Loop, J., and Hartree, R. (1989) Petrology and Li-Be-B geochemistry of muscovite-biotite granite and associated pegmatite near Yellowknife, Canada. Contributions to Mineralogy and Petrology, 102, 174–190.

Lee, D.E., Kistler, R.W., Friedman, I., and van Loenen, R.E. (1981) Two-mica granites of Northeastern Nevada. Journal of Geophysical Research, 86(B11), 10607–10616.

London, D., Hervig, R.L., and Morgan, G.B., VI (1988) Melt-vapor solubilities and element partitioning in peraluminous granite-pegmatite systems: Experimental results with Macusani glass at 200 MPa. Contributions to Mineralogy and Petrology, 99, 360–373.

London, D., Morgan, G.B., VI, and Hervig, R.L. (1989) Vapor-undersaturated experiments with Macusani glass + H_2O at 200 MPa, and the internal differentiation of granitic pegmatites. Contributions to Mineralogy and Petrology, 102, 1–17.

London, D., Morgan, G.B., VI, Babb, H.A., and Loomis, J.L. (1993) Behavior and effects of phosphorous in the system Na_2O-K_2O-Al_2O_3-SiO_2-P_2O_5-H_2O at 200 MPa (H_2O). Contributions to Mineralogy and Petrology, 113, 450–465.

Mahood, G., and Hildreth, W. (1983) Large partition coefficients for trace elements in high-silica rhyolites. Geochimica et Cosmochimica Acta, 47, 11–30.

Mansker, W.L., Ewing, R.C., and Keil, K. (1979) Barian-titanian biotites in nephelinites from Oahu, Hawaii. American Mineralogist, 64, 156–159.

Merrill, R.B., Robertson, J.K., and Wyllie, P.J. (1970) Melting reactions in the system $NaAlSi_3O_8$-$KAlSi_3O_8$-SiO_2-H_2O to 20 kilobars compared with results for the feldspar-quartz-H_2O and rock-H_2O systems. Journal of Geology, 78, 558–569.

Michael, P.J. (1988) Partition coefficients for rare earth elements in mafic minerals of high silica rhyolites: The importance of accessory mineral inclusions. Geochimica et Cosmochimica Acta, 52, 275–282.

Miller, C.F., Stoddard, E.F., Bradfish, L.J., and Dollase, W.A. (1981) Composition of plutonic muscovite: Genetic implications. Canadian Mineralogist, 19, 25–34.

Morgan, G.B., VI (1986) Alteration of amphibolitic wallrocks around the Tanco rare element pegmatite, Manitoba. Master's thesis, University of Oklahoma, Norman, Oklahoma.

Munoz, J.L. (1984) F-OH and Cl-OH exchange in micas with applications to hydrothermal ore deposits. In Mineralogical Society of American Reviews of Mineralogy, 13, 469–493.

Nabelek, P.I. (1986) Trace-element modeling of the petrogenesis of granophyres and aplites in the Notch Peak granitic stock, Utah. American Mineralogist, 71, 460–471.

Nash, W.P., and Crecraft, H.R. (1985) Partition coefficients for trace elements in silicic magmas. Geochimica et Cosmochimica Acta, 49, 2309–2322.

Neiva, A.M.R., and Gomes, M.E.P. (1991) Geochemistry of the granitoid rocks and their minerals from Lixa do Alvao-Alfarela de Jales-Tourencinho (Vila Pouca de Aguiar, northern Portugal). Chemical Geology, 89, 305–327.

Neiva, A.M.R., Neiva, J.M., and Parry, S.J. (1987) Geochemistry of the granitic rocks and their minerals from Serra da Estrela, Central Portugal. Geochimica et Cosmochimica Acta, 51, 439–454.

Patiño Douce, A.E., and Johnston, A.D. (1991) Phase equilibria and melt productivity in the pelitic system: Implications for the origin of peraluminous granitoids and aluminous granulites. Contributions to Mineralogy and Petrology, 107, 202–218.

Peterson, J.W., Chacko, T., and Kuehner, S.M. (1991) The effects of fluorine on the vapor-absent melting of phlogopite + quartz: Implications for deep-crustal processes. American Mineralogist, 76, 470–476.

Philpotts, J.A., and Schnetzler, C.C. (1970) Phenocryst matrix partition coefficients for K, Rb, Sr, and Ba, with applications to anorthosite and basalt genesis. Geochimica et Cosmochimica Acta, 34, 307–322.

Pichavant, M., Valencia Herrera, J., Boulmier, S., Briqueu, L., Joron, J.L., Juteau, M., Marin, L., Michard, A., Sheppard, S.M.F., Treuil, M., and Vernet, M. (1987) The Macusani glasses, SE Peru: Evidence of chemical fractionation in peraluminous magmas. In Geochemical Society Special Publication, 1, 359–373.

Pichavant, M., Kontak, D.J., Valencia Herrera, J., and Clark, A.H. (1988) The Miocene-Pliocene Macusani volcanics, SE Peru I: Mineralogy and magmatic evolution of a two-mica aluminosilicate-bearing ignimbrite suite. Contributions to Mineralogy and Petrology, 100, 300–324.

Ragland, P.C. (1989) Basic analytical petrology, 369 p. Oxford University Press, New York.

Rapp, R.P., and Watson, E.B. (1986) Monazite solubility and dissolution kinetics: Implications for the thorium and light rare earth chemistry of felsic magmas. Contributions to Mineralogy and Petrology, 94, 304–316.

Shearer, C.K., Papike, J.J., Simon, S.B., and Laul, J.C. (1986) Pegmatite-wallrock interactions, Black Hills, South Dakota: Interaction between pegmatite-derived fluids and quartz-mica schist wallrock. American Mineralogist, 71, 518–539.

Silva, M.M.V.G., and Neiva, A.M.R. (1990) Geochemistry of the granites and their minerals from Paredes da Beira-Penedono, northern Portugal. Chemical Geology, 85, 147–170.

Sisson, T.W. (1991) Pyroxene-high silica rhyolite trace element partition coefficients measured by ion microprobe. Geochimica et Cosmochimica Acta, 55, 1575–1585.

Skjerlie, K.P., and Johnston, A.D. (1992) Vapor-absent melting at 10 kbar of a biotite- and amphibole-bearing tonalitic gneiss: Implications for the generation of A-type granites. Geology, 20, 263–266.

Stewart, D.B. (1978) Petrogenesis of lithium-rich pegmatites. American Mineralogist, 63, 970–980.

Storre, B. (1972) Dry melting of muscovite + quartz in the range P_s=7 kb to P_s=20 kb. Contributions to Mineralogy and Petrology, 37, 87–89.

Storre, B., and Karotke, E. (1971) An experimental determination of the upper stability limit of muscovite + quartz in the range 7–20 kb water pressure. Neues Jahrbuch für Mineralogie Monatshefte, 237–240.

——— (1972) Experimental data on melting reactions of muscovite + quartz in the system K_2O-Al_2O_3-SiO_2-H_2O to 20 kb water pressure. Contributions to Mineralogy and Petrology, 36, 343–345.

Tuttle, O.F., and Bowen, N.L. (1958) Origin of granite in light of experimental studies in the system $NaAlSi_3O_8$-$KAlSi_3O_8$-SiO_2-H_2O. Geological Society of America Memoir, 74, 153 p.

Velde, B. (1966) Upper stability of muscovite. American Mineralogist, 51, 924–929.

Vielzuef, D., and Holloway, J.R. (1988) Experimental determination of the fluid-absent melting relations in the pelitic system. Contributions to Mineralogy and Petrology, 98, 257–276.

Walker, R.J., Hanson, G.N., Papike, J.J., O'Neil, J.R., and Laul, J.C. (1986) Internal evolution of the Tin Mountain pegmatite, Black Hills, South Dakota. American Mineralogist, 71, 440–459.

Walker, R.J., Hanson, G.N., and Papike, J.J. (1989) Trace element constraints on pegmatite genesis: Tin Mountain pegmatite, Black Hills, South Dakota. Contributions to Mineralogy and Petrology, 101, 290–300.

Watson, E.B., and Capobianco, C.J. (1981) Phosphorous and the rare earth elements in felsic magma: An assessment of the role of apatite. Geochimica et Cosmochimica Acta, 45, 2349–2359.

Watson, E.B., and Harrison, T.M. (1983) Zircon saturation revisited: Temperature and compositional effects in a variety of crustal magma types. Earth and Planetary Science Letters, 64, 295–304.

Webster, J.D., Holloway, J.R., and Hervig, R.L. (1987) Phase equilibria of a Be, U and F-enriched vitrophyre from Spor Mountain, Utah. Geochimica et Cosmochimica Acta, 51, 389–402.

White, A.J.R., and Chappell, B.W. (1983) Granitoid types and their distribution in the Lachlan Fold Belt, southeastern Australia. Geological Society of America Memoir, 159, 21–33.

Yoder, H.S., and Eugster, H.P. (1955) Synthetic and natural muscovites. Geochimica et Cosmochimica Acta, 8, 225–280.

Zen, E. (1988) Phase relations of peraluminous granitic rocks and their petrogenetic implications. Annual Reviews of Earth and Planetary Science, 16, 21–51.

Manuscript received October 20, 1994
Manuscript accepted July 24, 1995

Appendix

Electron microprobe analyses of glasses used two beam conditions to determine major- and minor-element oxide concentrations. The first condition consisted of a 15 μm spot size, a current of 2 nA, and an accelerating potential of 20 keV. Under these conditions we minimized K and Na migration; we noted alkali loss with beam currents as low as 5 nA. The second condition consists of 15 μm spot size, a current of 20 nA, and an accelerating potential of 20 keV. Two-sigma lower limits of detection (LLDs), diffracting crystals, and counting times on peak positions are tabulated in Appendix Table 1.

X-ray interferences were determined by scanning the wavelength-dispersive spectrometers across X-ray peaks on both standard materials and experimental charges. In all cases we were able to adequately separate X-ray peaks by judicious use of diffracting crystals. Background offsets were chosen at least 500 steps away from the peak centers. Because the Si$K\alpha,\beta$ peak is broad and close to the peak positions for Rb and Sr, a single background position for each element was chosen. The second background was defined by the slope of a line from the first background. The slope of the background counts for Sr was determined on samples not containing silica. Because all our Rb standards contain silica the slope was adjusted until the correct number of Rb$L\alpha$ counts was determined. Background-level X-ray counts for Sr and Rb on quartz confirmed that the peak positions were correctly placed. In all cases, minerals with simple chemical compositions were used as standards.

Trace-element analyses of Li, Rb, Ba, Sr, and Cs were performed by secondary ion mass spectrometry (SIMS) using the Cameca IMS 4f instrument operated by the University of New Mexico/Sandia National Laboratories Ion Microprobe Facility.

Analysis involved bombardment of the sample with primary O^- ions accelerated through a potential of 10 kV. A primary ion current of 1 nA was focused on the sample over a spot diameter of 10–15 μm. Sputtered secondary ions were energy filtered using a sample offset voltage of -75 V and an energy window of 20 V to eliminate effectively isobaric interferences. Each analysis involved repeated cycles of peak counting on $^{7}Li^{+}$, $^{23}Na^{+}$, $^{24}Mg^{+}$, $^{30}Si^{+}$, $^{85}Rb^{+}$, $^{88}Sr^{+}$, $^{133}Cs^{+}$, and $^{138}Ba^{+}$, as well as counting on a background position to monitor detection noise. The Na and Mg peaks were measured to provide Na and Mg concentrations as a check for glass contamination in mica and vice versa. Counting times were varied to achieve an analytical precision of a least 3% (typically 1–2%) on each element. Absolute concentrations of each element were calculated using empirical relationships of ratios of measured peak to $^{30}Si^{+}$ (normalized to known SiO_2 content) to element concentrations, as derived from measurements of documented standards. Mica analyses were referenced to CRPG standards MICA-Fe and MICA-Mg. Glass analyses were referenced to in-house rhyolite standards (DM0 and UTR-2).

The uncertainty in our microprobe measurements is quantified by the standard deviation about the mean, which is defined as the standard deviation divided by the square root of the number of analyses. The uncertainty in our reported distribution coefficients is taken from the equation (Ragland, 1989) $s = D^*[u/M)^2_{xl} + (u/M)^2_m]^{1/2}$ where s is the uncertainty in the distribution coefficient, u is the standard deviation about the mean for the oxide in the crystal (xl) or melt (m), M is the oxide in weight percent, and D is the distribution coefficient.

Appendix Table 1. Analytical conditions

Condition 1				Condition 2			
Element	LLD (wt%)	Crystal	*t* (s)	Element	LLD (wt%)	Crystal	*t* (s)
Si	0.11	TAP	90	Fe	0.02	LiF	20
Al	0.07	TAP	80	Ti	0.04	LiF	20
Na	0.07	TAP	10	Ni	0.04	LiF	20
K	0.06	PET	15	Rb	0.05	TAP	20
				Mn	0.04	LiF	10
				Ba	0.13	LiF	10
				Cs	0.11	LiF	20
				P	0.03	TAP	10
				Mg	0.02	TAP	10
				F	0.17	TAP	40
				Sr	0.07	PET	30
				Ca	0.07	PET	10

Note: LLD = lower limit of detection.